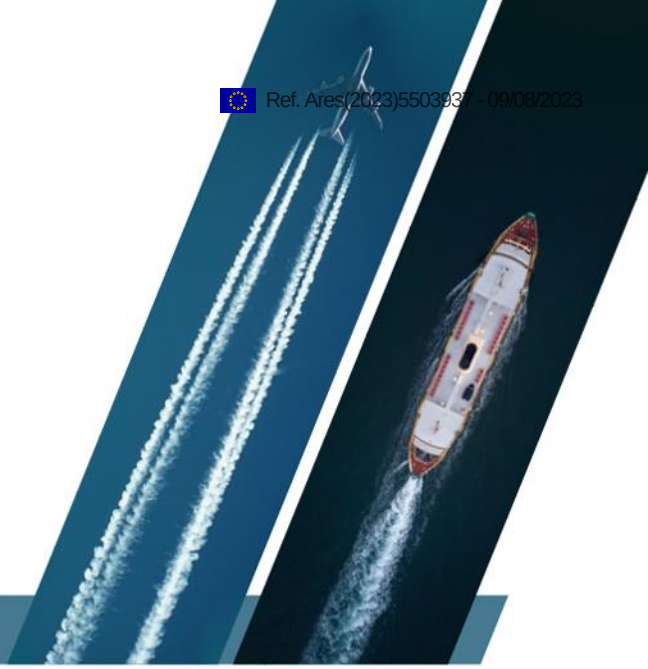

BioSFerA
Biofuel for biotravels

H2020-LC-SC3-2018-2019-2020
EUROPEAN COMMISSION
European Climate, Infrastructure and Environment Executive Agency (CINEA)

Biofuels production from **S**yngas
Fermentation for **A**viation and maritime use

Grant Agreement No 884208

Deliverable D6.1

Report on DFB Gasification Modelling

Document Details

Due date	May 31, 2023
Actual delivery date	June 20, 2023
Lead Contractor	SFW
Version	Final
Prepared by	Mohammad Ghazani, SFW Panagiotis Stamatopoulos, CERTH
Input from	Ville Nikkanen, VTT Esa Kurkinen, VTT Kari Myöhänen, LUT
Reviewed by	Juha Palonen, SFW, Kostis Atsonios (CERTH)

Document Details

X	PU - Public
	PP - Restricted to other programme participants (including the EC)
	RE - Restricted to a group specified by the consortium (including the EC)
	CO - Confidential, only for members of the consortium (including the EC)

Disclaimer of warranties

This project has received funding from the European Union's Horizon 2020 research and innovation programme under Grant Agreement No 884208. This document reflects only the author´s view and CINEA is not responsible for any use that may be made of the information it contains.

This document has been prepared by BioSFerA project partners as an account of work carried out within the framework of the EC-GA contract no 884208.

Neither Project Coordinator, nor any signatory party of BioSFerA Project Consortium Agreement, nor any person acting on behalf of any of them:

a. makes any warranty or representation whatsoever, express or implied,
   i. with respect to the use of any information, apparatus, method, process, or similar item disclosed in this document, including merchantability and fitness for a particular purpose, or
   ii. that such use does not infringe on or interfere with privately owned rights, including any party's intellectual property, or
   iii. that this document is suitable to any particular user's circumstance; or
b. assumes responsibility for any damages or other liability whatsoever (including any consequential damages, even if Project Coordinator or any representative of a signatory party of the BioSFerA Project Consortium Agreement, has been advised of the possibility of such damages) resulting from your selection or use of this document or any information, apparatus, method, process, or similar item disclosed in this document.

Abbreviations

CFB	Circulating Fluidized Bed
CFD	Computational Fluid Dynamics
DFB	Dual Fluidized Bed
EMMS	Energy Minimization Multi-Scale
KTGF	Kinetic Theory of Granular Flow

Contents

1 Executive Summary

This deliverable presents the modelling of the dual fluidized bed (DFB) gasification in Task 6.1. The primary objective was to develop a fast and reliable model system for studying DFB gasification. To achieve this, pilot-scale tests conducted by VTT were used as a basis for calibrating the model. Following calibration, the model was applied to simulate a full-scale DFB unit, thereby validating the design of the scaled-up unit.

Both the pilot-scale and full-scale DFB units operated on the same principle, with the gasifier and the oxidizer functioning as circulating fluidized bed reactors. In the pilot-scale tests, bark served as the fuel, and the bed material was a mix of sand (30%) and dolomite (“Myanit B”, 70%). In contrast, the full-scale unit used wood chips as fuel, with the bed material comprising sand (70%) and limestone (30%). The fuel input was approximately 120 kW at the pilot scale and 100 MW at the full scale.

CERTH developed a custom-made Energy Minimization Multi-Scale (EMMS) drag sub-model to enhance the accuracy of simulations under the specific operational conditions of the pilot-scale DFB unit. The fluid dynamics of the pilot gasifier were investigated using the Ansys Fluent multiphase model, which applies the Kinetic Theory of Granular Flow (KTGF). Both a standard drag model based on Wen-Yu drag and the EMMS drag model were tested to simulate the pilot-scale gasifier. While both model approaches satisfactorily simulated the measured pressure profiles, they largely underestimated the circulating rate and the solid concentration at the bottom of the gasifier. Additionally, the calculation times were long and subject to divergence problems.

To achieve practical and efficient calculation of the coupled reactors, a semi-empirical approach was selected. This approach involved setting the solid concentration profiles in the 3-D process model based on empirical data, including the share of bed materials, particle size distributions, and the total solid concentration profile derived from the pressure profile. The reaction submodels were calibrated based on the pilot-scale tests, and the same set of parameters were used for simulating each pilot-scale test. The modelled gas compositions and reactor temperatures aligned well with the measurements.

The calibrated model was then used to simulate a full-scale DFB unit. The initial reactor dimensions and the placement of feeds were adjusted based on the model results. The main objective of developing a fast and reliable model system for studying DFB gasification was successfully achieved. The calibrated model can be applied to study the full-scale unit under different process conditions.

2 Introduction

Indirect steam gasification is a promising technology for the production of clean and sustainable energy from biomass-based materials. It involves the conversion of organic carbonaceous materials into producer gas. The producer gas from the steam-blown gasifier is free from atmospheric nitrogen and mainly consists of combustible gases (CO, H_2, C_xH_y), water vapour, and carbon dioxide. The producer gas is further processed into syngas (synthesis gas), which mainly consists of carbon monoxide and hydrogen. Nowadays, the terms “producer gas” and “syngas” are often mixed and even the un-processed gas, which is exiting the gasifier is sometimes called as “syngas”. However, technically, syngas should refer to a gas mixture that has been processed and cleaned, typically to a higher quality than the initial producer gas. This is because syngas is used as a precursor for the production of other chemicals or fuels, and the removal of impurities and adjustment of gas composition are critical to these downstream processes.

A key feature of indirect steam gasification is the use of a dual fluidized bed (DFB) system, which consists of two interconnected reactors: a gasifier and an oxidizer (or combustor). The gasifier operates under reducing conditions to generate producer gas, while the oxidizer burns the residual char (or other combustibles such as light gas coming from other parts of the downstream process) to generate heat, which is then transferred to the gasifier through a circulating bed material (Figure 1).

The modelling of DFB gasification is a complex task due to the intricate interplay of fluid dynamics, heat transfer, and chemical reactions. Two main modelling approaches were applied in this study: the Energy Minimization Multi-Scale (EMMS) model for studying the fluid dynamics and a semi-empirical 3-D process model for comprehensive simulation of the DFB system.

The EMMS model, developed by CERTH, is a sophisticated drag sub-model that significantly enhances the accuracy of simulations under specific operational conditions. It accounts for sub-grid particle clustering mechanisms, thereby improving the accuracy of the drag exerted on the particles. This is crucial as conventional drag models tend to overestimate this force, leading to low-accuracy simulations. The EMMS model provides a “drag calculation map” that varies with different operating conditions, such as particle and gas properties. Correcting the conventional drag models by EMMS improves the accuracy of the CFD simulations.

The semi-empirical, steady-state 3-D process model offers a practical and efficient approach to simulate the coupled reactors. The empirical nature of the model requires that valid experimental data is available for calibrating the different submodels, which determine e.g. the fluid dynamics of solids and the various heterogenous and homogeneous reactions. For this purpose, a set of pilot-scale DFB tests carried out at VTT was applied. The calibrated model was then used to simulate a full-scale DFB unit.

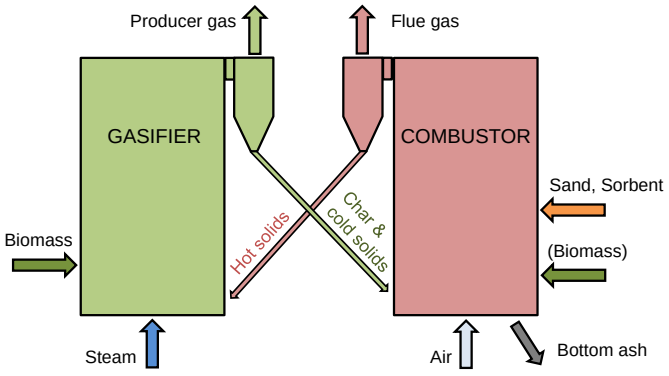

Figure 1. The basic principle of indirect steam gasification of biomass (Myöhänen et al., 2018).

3 EMMS model

Mathematical modelling and numerical simulation play an essential role in guiding the optimization design, up-scaling, and operational optimization of gas-solid fluidized bed reactors. These reactor applications can be found in industrial processes such as, coal combustion, flue gas desulfurization e.c.t. The complex nature of these reactors, involving multiscale, multipattern, and multiphase coupling, necessitates the use of sophisticated mathematical models and numerical simulation (Li et al., 2013). Therefore, it is crucial to develop dependable Computational Fluid Dynamics (CFD) models that can accurately predict the governing hydrodynamic phenomena in gas-solid flows, while minimizing computational cost. Gas-solid flows, such as in fluidized beds (FB), display heterogeneity across a wide range of spatial and temporal meso-scale structures. Generally, these spatiotemporal multi-scale structures significantly influence the behaviour of multiphase flows, impacting the accuracy of numerical simulations (FB) boilers. These structures are highly non-linear and prone to instability. The calculation of drag force exerted by the gas phase on the solid particles is a critical aspect affecting the numerical accuracy of the two-fluid model, and perhaps the most significant source of inaccuracy. Several conventional drag models have been developed i.e. by Syamlal and O'Brien (Syamlal, 1987), Wen and Yu (Wen and Yu, 1966) and Gidaspow (Gidaspow, 1994). These drag models are limited to uniform conditions, since they cannot consider the flow heterogeneity resulted from the existence of mesoscale structure within the computational grid-scale and its effects on drag. In the last decades in fluidized bed simulations the development of the theoretical approach of using the Theory of Energy Minimization Multiscale (EMMS) to establish a heterogeneous drag model (Chen, 2015). The EMMS scheme addresses the meso-scale structural influence on the calculation of the drag coefficient in each computational cell (Wang et al., 2008). It is based on multi-scale modelling strategy that investigates controlling mechanisms at smaller scales to formulate phenomena occurring at higher scales (macro-scale) (Li and Kwauk, 2003).

3.1 EMMS Model in-house development

In this task, an EMMS gas-solid drag force model developed by CERTH (Zeneli et al., 2015) is the state-of-the-art Energy Minimization Multi-Scale Scheme (EMMS) based on the work of Wang et al (Wang and Li, 2007) with several modifications on specific closure equations (e.g. the cluster diameter). The results of which will be integrated into the CFB 3D code developed by SHI-FW and LUT for a higher level of accuracy of the predicted pressure profile and flow patterns. This EMMS version developed by CERTH has been already validated in previous EU-funded projects, e.g. SCARLET (European Commission, 2017) and FlexFlores (FlexFlores, 2019). In the framework of BioSFerA Project (BioSFerA, 2020), this type of model should be re-tuned for the specific operating conditions of the gasifier/oxidizer units through a custom-built FORTRAN code that solves a system of nonlinear equations and its results are the heterogeneity index (H_d) values for several gas-solid slip velocities and solid volume fractions. Figure 2 presents a schematic diagram of the EMMS model inputs (operating conditions) and outputs (H_d). More specifically, the input parameters of the EMMS model are the solid particles density and diameter, the gas density and viscosity, and, the reactor diameter.

The main output is the dimensionless factor H_d, the so-called heterogeneity index, which is the ratio of the drag force calculated by the conventional model of Wen & Yu to the drag force calculated by the EMMS model:

$$H_d = \frac{F_{Wen\&Yu}}{F_{EMMS}} \quad 3.1$$

The calculation of the F_{EMMS} force, utilizing the EMMS scheme, and the subsequent determination of the heterogeneity index H_d, are obtained by solving a set of analytical, empirical and semi-empirical equations explained in detail by Zeneli et al. (Zeneli et al., 2015).

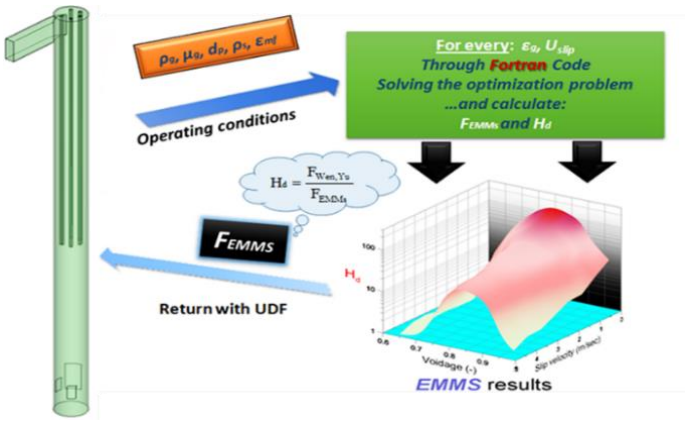

Figure 2. EMMS model integration in a CFD model.

3.2 EMMS results

EMMS code has been run for both the gasifier and the oxidizer operating conditions. Additionally, in both reactors the main solids inventory is a share of sand and Myanite, and, thus, the model has been run for these two solid material properties. The input parameters of the EMMS model are summarized in Table 1.

		Myanite		Sand	
Parameter	**Symbol, units**	**Gasifier**	**Oxidizer**	**Gasifier**	**Oxidizer**
Reactor diameter	D_r, m	0.15	0.15	0.15	0.15
Particle diameter	d_p, μm	480	480	355	355
Gas density	ρ_g, kg/m^3	0.28	0.36	0.28	0.36
Solid density	ρ_s, kg/m^3	2500	2500	2500	2500
Gas viscosity	μ_g, kg m^{-1}s^{-1}	3.83E-5	4.19E-5	3.83E-5	4.19E-5

Table 1. EMMS model input parameters.

Mean values of the different gas-solid properties inside the two reactors are used. The gas/solid properties and reactor diameter are based on data received from VTT and SHI-FW/LUT. The particle size distribution is not taken into account for the inert material as it increases considerably the computational cost (monosized approach for particles diameter). The mean diameter is calculated as harmonic mean diameter:

$$\overline{d_p} = \frac{1}{\sum_i^{all}\left(\frac{x}{d_p}\right)_i} \qquad 3.2$$

The set of the EMMS equations is solved through a custom-built FORTRAN code for specific values of the gas–solid slip velocity u_{slip} (0.5, 1, 2, 3, 4, 5) and for discrete values of the gas volume fraction ε_g within the range of ε_{mf} (0.6) to ε_{max} (0.997). The range of volume fraction $\varepsilon_g \in [0.6,1]$ is divided into three sub-domains to achieve higher accuracy by interpolating the heterogeneity index H_d using 6th order polynomials.

$$H_d(\varepsilon_g) = a_0 + a_1\varepsilon_g + a_2\varepsilon_g^2 + a_3\varepsilon_g^3 + a_4\varepsilon_g^4 + a_5\varepsilon_g^5 + a_6\varepsilon_g^6 \quad 3.3$$

The first area $\varepsilon_g \in [\varepsilon_{mf}, 0.82]$ (Area C, Figure 3) and the second area $\varepsilon_g \in [0.82, 0.95]$ (Area B), describe the dense conditions and the dilute area, where $\varepsilon_g \in [0.95, \varepsilon_{g_{critical}}]$, (Area A). For very dilute conditions, i.e. Area A, H_d is predicted to be unity. This is expected since highly dilute conditions hinder the formation of clusters. The particle loading at which the transition from heterogeneity to homogeneity occurs cannot be easily predicted. To this end, a second order polynomial of $\varepsilon_{g_{critical}}$ as a function of u_{slip} must be defined as a constrain in the CFD code. This polynomial, occurs in each case, by fitting the critical values of ε_g of each gas–solid slip velocity:

$$\varepsilon_{g_{critical}}(u_{slip}) = b_o + b_1 u_{slip} + b_2 u_{slip}^2 \quad 3.4$$

Figure 3 and Figure 4 present the results of the EMMS model (back dots) with the interpolated polynomial, (solid lines).The divided areas of volume fraction ε_g are depicted with different colors, i.e. Area A, Area B and Area C with green, blue and red solid lines, respectively. In Table 2 and Table 3, the high accuracy of the fitted polynomial is confirmed, since the statistical values of R-squared is almost equals to unity.

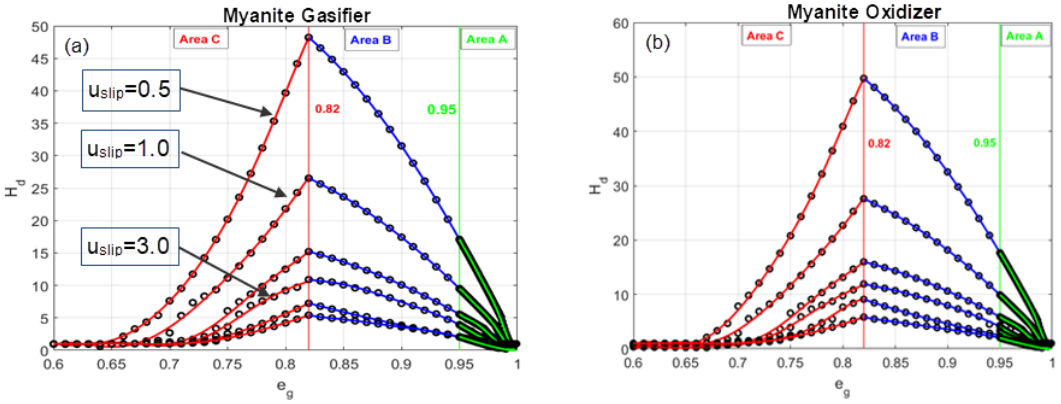

Figure 3. EMMS model results and interpolation of H_d values for Myanite in (a) gasifier and (b) oxidizer reactor.

Myanite						
u_{slip} [m/s]	Gasifier			Oxidizer		
	Area C	Area B	Area A	Area C	Area B	Area A
0.5	0.999	1	0.999	0.9998	1	0.9984
1	0.997	1	0.999	0.9998	1	0.9999
2	0.995	0.999	0.998	0.9981	0.9997	0.9995
3	0.995	0.999	0.999	0.9929	0.9984	0.9988
4	0.998	0.998	0.996	0.9969	0.9992	0.9992
5	0.998	0.999	0.997	0.9993	0.9997	0.9987

Table 2. R-squared values of fitting polynomial.

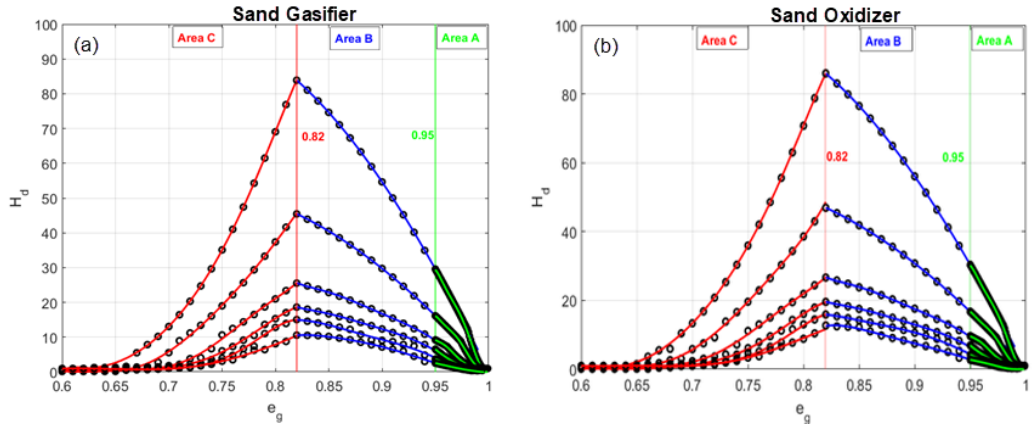

Figure 4. EMMS model results and interpolation of H_d values for Sand in (a) gasifier and (b) oxidizer reactor.

Sand						
u_{slip} [m/s]	Gasifier			Oxidizer		
	Area C	Area B	Area A	Area C	Area B	Area A
0.5	0.999	1	0.999	1	0.998	0.999
1	0.998	0.999	0.999	0.999	1	0.999
2	0.997	0.999	0.999	0.999	0.999	0.999
3	0.998	0.999	0.998	0.997	0.999	0.998
4	0.997	0.993	0.998	0.998	0.999	0.999
5	0.995	0.997	0.997	0.996	0.998	0.998

Table 3. R-squared values of fitting polynomial, Sand.

4 Description of the 3-D model

The 3-D model has been originally developed for circulating fluidized bed combustion (Myöhänen and Hyppänen, 2011). Since then, the model has been extended to handle different multiphase energy conversion processes, such as bubbling fluidized bed combustion, oxygen-fired CFB combustion, calcium looping, and gasification (Koski et al., 2012; Myöhänen et al., 2018, 2014; Nikku et al., 2021, 2016, 2014; Parkkinen et al., 2017). In the model, the reactors are modelled three-dimensionally while other connected systems (e.g. cyclones and solids looping systems) are modelled by black-box-models, which exchange data with the 3-D reactor models (Figure 5).

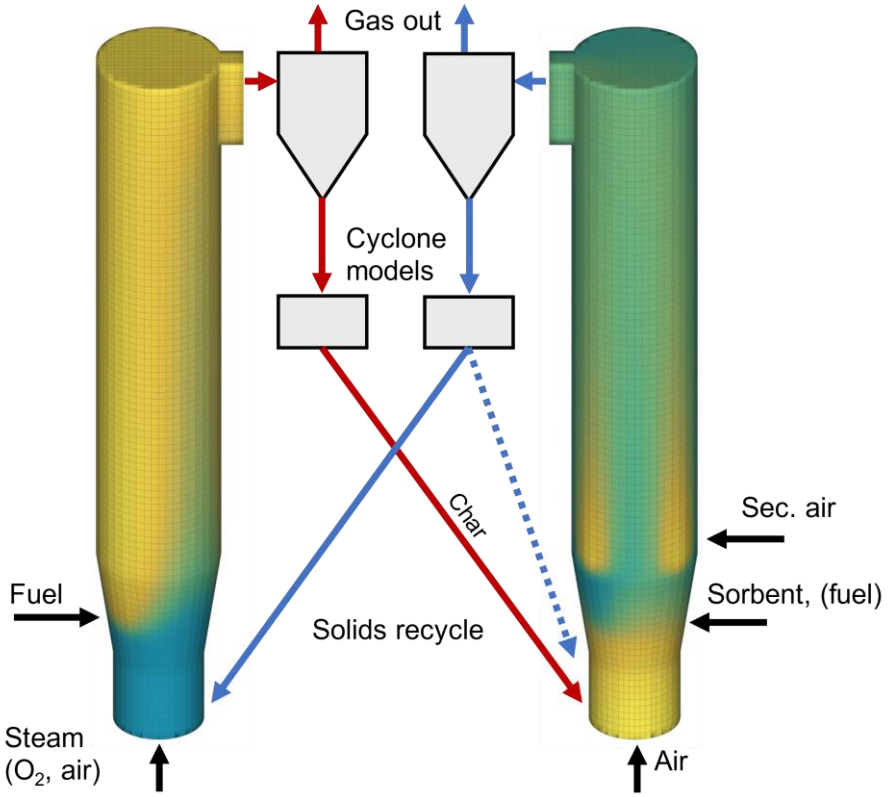

Figure 5. Illustration of the 3-D model showing the surface mesh of large-scale DFB reactors.

Typically, the gasifier is fluidized by steam; however, in the pilot-scale tests, additional oxygen and/or air were introduced to elevate the gasifier's temperature. The fuel, predominantly fed into the gasifier, undergoes evaporation and devolatilization. A portion of the char is consumed in heterogeneous gasification reactions. The residual char is transferred to the air-blown oxidizer, where it combusts alongside any extra fuel introduced. The oxidizer is also the point of entry for the sorbent and sand. At the oxidizer's high temperature, the sorbent undergoes calcination. Secondary air is introduced after the frustrum to ensure good combustion efficiency. The heated bed material is transferred from the oxidizer to the gasifier, providing the necessary heat for the gasification process.

The solved variable systems include:

- fluid dynamics of solids and gas,
- heterogeneous fuel and sorbent reactions,
- homogeneous reactions,
- heat transfer within fluidized bed and to surfaces,
- separate submodels for separators and looping systems.

The reactors are modelled three-dimensionally using a control volume method to discretize and solve various balance equations under steady-state conditions. While the original model utilized a fully orthogonal mesh with hexahedral calculation cells, this project introduced a new feature of body-fitted meshing using the cut-cell method (see example surface meshes in Figure 5). The balance equations are solved using the first-order upwind differencing scheme and the Gauss-Seidel method with successive overrelaxation.

The model's boundary conditions encompass different gas and solid feeds, represented as local volumetric source terms. To specify heat transfer to outer walls and potential internal heat exchangers, the cold side temperature of the wall and the wall structure (including thickness and thermal conductivity of the wall and any refractory lining) are defined. Additionally, the model allows for the setting of local heat sources and sinks. This feature was utilized to account for the electrical heating used in the pilot-scale tests.

Solid feeds can include fuels, sorbents (such as limestone), and inert make-up materials (like sand). The model is not limited by the number of each solid feed material, enabling the simulation of multi-fuel and multi-sorbent cases. All solid materials can be divided into up to six particle size fractions to simulate continuous particle size distributions and particle comminution. Gaseous feeds can be freely defined in terms of feed location, temperature, and composition.

Input data is supplied via a text file, generated using an Excel-based application developed specifically for this model. This file includes all necessary data for calculation, including boundary conditions, material properties, and geometric and meshing data

Before invoking the iterative solver, the calculation data must be initialized. This can be achieved either through an initialization subroutine or by utilizing existing data as the starting state. The solver is divided into different modules, each dedicated to solving specific variable systems. The execution of these solver modules can be user-controlled. For instance, the solution of the energy equation can be bypassed if desired. This feature can be particularly useful during the initial stages of iterations to prevent excessively low or high temperatures before the reaction rates and heat transfer have stabilized.

The simulation of interconnected reactors is managed by initiating a separate model session for each reactor. Data exchange between the reactors occurs at the beginning and end of the iteration round. For example, the gasifier model calculates the composition and mass flow discharged from the gasifier and fed into the oxidizer. The oxidizer model then reads this data and solves the discharge flow returning to the gasifier.

The iterations cease when either the desired convergence level is achieved, the defined number of iterations is reached, or the process is manually stopped. Subsequently, the output data is recorded. The 0D (overall) and 1D profile data are written to text files, which are further processed in the Excel application. The 3D data is written to binary files, which can be examined using visualization software.

4.1 Solid concentration fields and solid flow fields

In the population balance approach, the continuous particle size distribution is discretized into particle size fractions. Each particle size fraction then represents a group of particles within a defined range (e.g. 125 – 180 µm). In this model, all solid materials (including combustible fuel, ash, sand, and limestone) can be divided into up to six particle size fractions. The comminution of solids, or the reduction of particle size, is simulated using a rate model where the mass change is proportional to the mass. The mass change due to comminution from particle size i to particle size j is expressed as:

$$q_{m,Cij} = k_{C,ij} m_i \qquad 4.1$$

In Eq. 4.1, $k_{C,ij}$ is a comminution coefficient, which is defined in the input data as a matrix between each fraction. Figure 6 illustrates the comminution paths from coarser to finer fractions, with comminution coefficients determined between each size fraction. The model can also simulate the agglomeration of particles. However, particle size typically decreases due to mechanical wear of particles, temperature shocks, and the effects of chemical reactions (e.g., the breaking of char particles during combustion)..

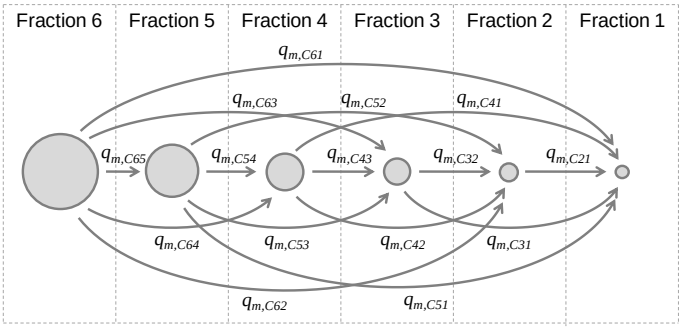

Figure 6. Comminution paths from coarser to finer fractions.

The comminution effects have been included to three-dimensional transport equations of solids. The mass of solids in cell volume dV can be expressed with volume fraction of solids ε_s and material density ρ_s for each particle size fraction i:

$$m_{i,dV} = \int_V \varepsilon_{s,i}\rho_{s,i}\, dV \qquad 4.2$$

The steady-state total mass change due to comminution for particle size fraction i in cell volume dV includes comminution from fraction i to other size fractions j and comminution from other fractions j to size fraction i. The net mass flow due to comminution for fraction i is then:

$$\int_V q'''_{m,Ci}\, dV = \int_V \sum_{j,j\neq i} k_{C,ij}\varepsilon_{s,i}\rho_{s,i}\, dV - \int_V \sum_{j,j\neq i} k_{C,ji}\varepsilon_{s,j}\rho_{s,j}\, dV \qquad 4.3$$

The solid concentration profiles inside the reactor are set by empirical correlations or by using the externally solved concentration fields. The externally solved concentrations fields originate typically from multiphase CFD calculation, using either Eulerian-Eulerian (e.g. KTGF model) or Lagrangian-Eulerian (e.g. DDPM model) simulation approach (Adamczyk et al., 2018). With externally solved concentration fields, the local solid concentration can be set directly by interpolation of the fields solved by CFD. When empirical correlations are applied, the solid concentration fields are simplified. The primary feature of the averaged solids flow (steady-state) in a CFB reactor is the core-annulus flow. In the core, the up-flow of solids exhibits a nearly flat solids flux profile, while at the wall layer, the solids descend in a denser flow. This model utilizes this feature by assuming a flat lateral distribution of solids in the core of the CFB. The denser wall layer flow is simulated by a superimposed wall layer model. The volume fraction of solids at the wall layer is determined as a function of the local average volume fraction of solids (ε_s) across the cross-section of the furnace:

$$\varepsilon_{s,wl} = \varepsilon_{max}\left[1 - \exp\left(-a\frac{\varepsilon_s}{\varepsilon_{max}}\right)\right] \qquad 4.4$$

In large-scale CFBs, the thickness of the wall layer is typically in the order of 0.1...0.2 m. In a small scale, a similar clear wall layer is not formed, and in the simplified model, the solid concentration in the steady-state can be assumed to be flat in the horizontal direction.

The solid concentration can be approximated from the measured pressure gradient:

$$\rho_s(h) = \frac{-\nabla p(h)}{g} \quad 4.5$$

The vertical solid concentration is set to follow the equation derived from a formula given by Johnsson and Leckner (Johnsson and Leckner, 1995).

$$\rho_s(h) = \left[\rho_{s,btm} - \rho_{s,top} exp(c_{di} H_t)\right] exp(-c_{tr} h) + \rho_{s,top} exp[c_{di}(H_t - h)] \quad 4.6$$

In the pilot-scale tests, the bed material consisted of Myanit B (70%) and sand (30%). The particle size distribution of these materials was provided by VTT (Figure 7).

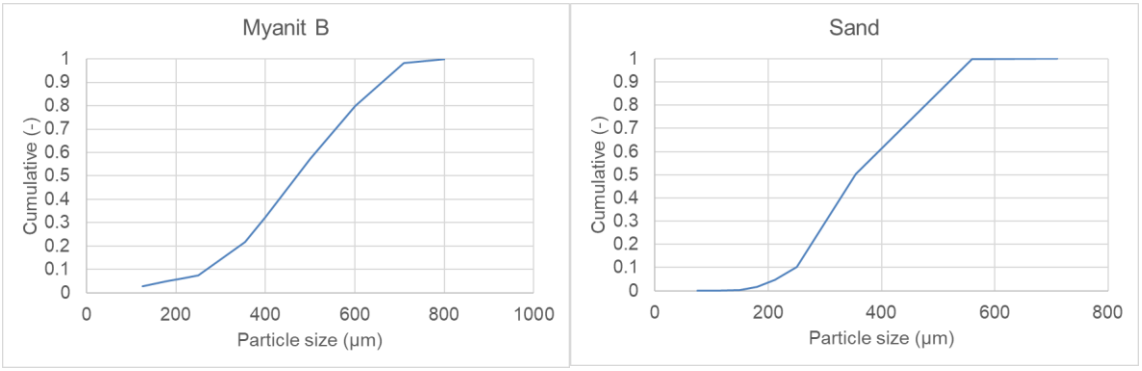

Figure 7. Cumulative particle size distributions.

In the initial model studies, the bed material was set to consist of Myanit and sand with the average particle size of 480 µm and 355 µm, respectively. The choice of applying only two particle size fractions was due to the need to reduce the number of solid phases for CFD modelling so that the calculation times would have been feasible. However, this approach resulted in too low circulation rates. After analyzing the CFD results, it became evident, that the bed material should consist of a coarse bed and a fine bed. The circulation rate of the coarse bed is very low, while most of the circulating material consists of the fine bed material. For the final calculations, the bed material was set to consist of coarse and fine bed material, the share of each determined from the measured particle size distributions (Figure 8). The mean particle sizes for the coarse section and the fine section were defined as harmonic mean diameters (Eq. 3.2). With this approach, the particle size of the two size fractions was set to 513 µm and 241 µm.

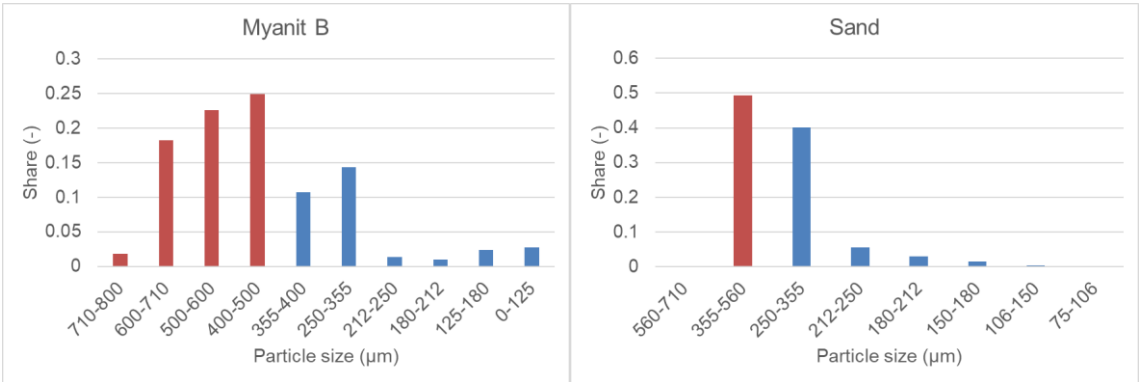

Figure 8. Range-specific particle size distributions. Coarse sections marked as red, fine sections as blue.

The parameters of the solid concentration profiles (Eq. 4.6) were set based on the total solid concentration profile, which was determined from the pressure profile. Figure 9 presents the solid concentration fields of fine and coarse bed materials and the total solid concentration compared with the profile determined from pressure measurements of the test case 18/26E.

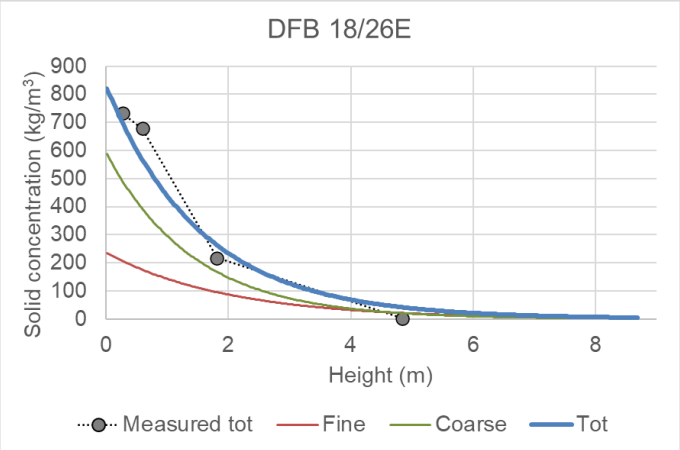

Figure 9. Solid concentration of fine and coarse bed materials and the total concentration compared with the experimental profile.

Similar to the solid concentration profiles, the velocity field of bed materials is either solved externally with CFD or within the 3D code. For solving the velocity field within the code, a modified potential approach is applied. This is a steady-state description of the flow field without the effects of vortices or transient mixing of solids. The local mixing effects due to vortices and fluctuating flow are considered by dispersion terms.

A flow potential P_{fs} is defined according to Eq. 4.7, i.e. the gradient of P_{fs} is equal to mass flux of solids. The continuity equation for total solids includes convection, a source term, and a reaction term (Eq. 4.8).

$$\varepsilon_s \rho_s \mathbf{v}_s = \nabla P_{fs} \tag{4.7}$$

$$\oint_A \varepsilon_s \rho_s \mathbf{v}_s \cdot d\mathbf{A} = \int_V \phi_s''' \, dV + \int_V R_s''' \, dV \tag{4.8}$$

The source term includes all the local solid sources and sinks, e.g. internal circulation of solids, solids flow from other reactor(s) and sinks due to bottom ash flow. The discharge solids flow is taken from the circulating material before it enters back to the reactor, i.e. it affects the circulating mass flow source. The discharge ratio is defined by user input. The reaction rate term includes the mass changes due to different reactions. The potential difference across the furnace outlet faces is set based on the determined constant outlet velocity, which comes from the overall mass balance. Combining the above equations, the potential field P_{fs} is solved, after which the solid velocity field is defined from Eq. 4.8.

The bottom ash is removed from the furnace at the specified locations and according to the solved mass balance. The composition of the bottom ash flow depends on the composition of solids at the bottom discharge points. However, in the modelled pilot and full-scale cases, the bottom ash flow rate was close to zero (which was the condition in the pilot scale tests as well).

Should the solid flow field be calculated using external CFD simulations, the CFD-derived fields cannot be directly utilized. This is because the external CFD calculations do not typically include chemical reactions due to high computational cost. More importantly, the time-averaged CFD-fields in general do not satisfy the mass balance exactly due to various reasons (e.g. due to calculation inaccuracies). Thus, using the CFD-fields directly would

result in mass balance errors – both locally and in the overall model. Consequently, an additional correction term is introduced to the potential flow equation, which "guides" the solved flow field towards the externally solved flow field:

$$\varepsilon_s \rho_s \mathbf{v}_s = \nabla P_{fs} + \beta_{CFD} \varepsilon_s \rho_s (\mathbf{v}_{CFD} - \mathbf{v}_s) \quad 4.9$$

The potential flow equation is then combined with the continuity equation (Eq. 4.8), which then ensures that the solved flow field satisfies the mass balance.

4.2 Pressure and gas flow fields

The solution of the gas flow fields is based on defining the continuity of gas and a simplified momentum balance for gas, in which the momentum exchange between the solids and gas is defined by a macroscopic drag term β_m:

$$\oint_A \varepsilon_g \rho_g \mathbf{v}_g \cdot d\mathbf{A} = \int_V \phi_g''' \, dV + \int_V R_g''' \, dV \quad 4.10$$

$$\int_V \beta_m \varepsilon_s \rho_s (\mathbf{v}_g - \mathbf{v}_s) \, dV = -\int_V \varepsilon_g \nabla P \, dV \quad 4.11$$

The continuity equation includes terms for convection (left side), sources, and reactions. The source term includes the different gas feeds as volumetric sources. Thus, for example, the penetration of gas jets is not solved in the model but must be provided based on measurements or additional CFD modelling. The model applies a relatively coarse calculation mesh, which does not allow for the solution of narrow and turbulent jet streams. The reaction term includes sources and sinks due to different heterogeneous reactions. In the momentum equation, the drag force (left side) is assumed equal to the force due to the pressure gradient. Combining the above equations, the pressure *P* is solved, after which the gas velocity field is defined from the momentum equation. The solved velocity field is the net velocity of the gas. In addition, the gases are mixing by dispersion, which is considered when solving the gas species.

4.3 Composition of fuel

The fuel is divided into char, volatiles, tar, moisture and ash by proximate analysis. The total elemental composition of the burning fuel (char, volatiles, and tar) is determined by ultimate analysis. The tar is assumed to consist of toluene (C_7H_8). In reality, the tar is a very complex combination of many heavy hydrocarbons, but with this simple approach, the share of tar-forming compounds in the producer gas can be approximated.

The composition of char is defined by empirical correlations as mass ratios :

$$\frac{H_{char}}{H_{tot}} = 0.52 \exp\left[-33 \left(\frac{H}{C}\right)\right] \quad 4.12$$

$$\frac{N_{char}}{N_{tot}} = 0.088 \, w_{char,daf}^{0.6} \left(\frac{H}{C}\right)^{-0.6} \quad 4.13$$

$$\frac{S_{char}}{S_{tot}} = 0.14 \, w_{char,daf}^{0.2} \left(\frac{H}{C}\right)^{-0.6} \quad 4.14$$

Oxygen is assumed to exist only in the volatiles. The composition of volatiles is calculated from the balance based on the ultimate analysis.

For the formation of the volatile species, following procedure is applied:

1. Elemental sulphur in volatile is used to form H_2S.
2. Elemental nitrogen in volatile is used to form NH_3.
3. Elemental oxygen in volatile is used to form CO and CO_2 in molar fraction of $\gamma_1 = n_{CO}/(n_{CO} + n_{CO_2})$.
4. Leftover carbon in volatile after forming CO and CO_2 is used to form hydrocarbons CH_4 and C_2H_4 in carbon molar fraction of $\gamma_2 = n_{C,CH_4}/(n_{C,CH_4} + n_{C,C_2H_4})$.
5. Leftover hydrogen in volatile after forming CH_4, C_2H_4, H_2S and NH_3 is used to form H_2.

The overall modelling of the fuel, decomposition paths, and the reactions is illustrated in Figure 10.

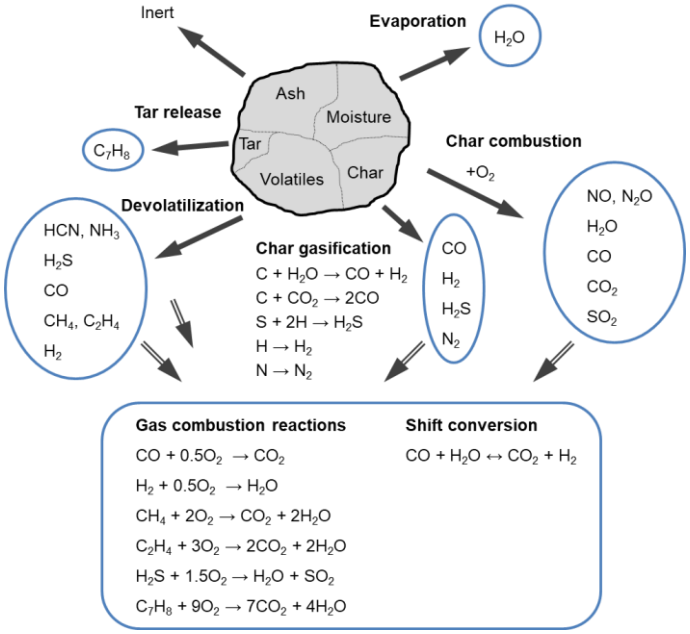

Figure 10. Illustration of the fuel decomposition and reactions.

In pilot-scale tests, the used feedstock fuel was bark, while for the full-scale unit, the fuel was considered as wood chips. The higher heat values in dry basis for bark and wood chips were 20 066 kJ/kg and 20 800 kJ/kg, respectively. Table 4 compares the fuel compositions and their respective main products. As both fuels are wood-based, the differences are relatively minor.

It should be underlined, that in steam-blown gasification, the composition of the producer gas is mostly determined by the devolatilization. Thus, the decomposition submodel has a decisive role in the overall modelling of the gasification.

Fuel	Bark (pilot)	Wood chips (full-scale)
Proximate analysis (wt-%, as rec.)		
Char	17.49	17.10
Volatiles	66.73	65.05
Moisture	11.20	15.00
Ash	2.58	0.85
Tar	2.00	2.00
Ultimate analysis (wt-%, daf)		
C	53.04	51.31
H	5.97	6.06
N	0.31	0.40
S	0.04	0.01
O	40.64	42.21
Char composition (kg/kg,char)		
C	0.9850	0.9851
H	0.0035	0.0030
N	0.0108	0.0118
S	0.0007	0.0002
O	0.0000	0.0000
Volatile composition (kg/kg,vol)		
C	0.4112	0.3891
H	0.0745	0.0758
N	0.0011	0.0020
S	0.0003	0.0001
O	0.5129	0.5331

Table 4. Fuel compositions.

4.4 Fuel flow field

The three-dimensional transport equations are defined for continuity of char, volatiles, moisture, and tar and solved for each particle size fraction. The continuity equation for particle size fraction *i* of char is defined as follows:

$$\oint_A \varepsilon_{char,i}\rho_{char}\mathbf{v}_{f,i}\cdot d\mathbf{A} - \oint_A D_{f,i}\nabla\left(\varepsilon_{char,i}\rho_{char}\right)\cdot d\mathbf{A} = \int_V \phi'''_{char,i}\,dV - \int_V R'''_{char,i}\,dV - \int_V \sum_{j,j\neq i} k_{C,char,ij}\varepsilon_{char,i}\rho_{char}\,dV + \int_V \sum_{j,j\neq i} k_{C,char,ji}\varepsilon_{char,j}\rho_{char}\,dV \quad (4.15)$$

The continuity equation is defined similarly for other reacting components: volatiles, moisture, and tar (replacing the appropriate variables in Eq. 4.15).

The convective mixing of reacting fuel is modelled by defining a momentum equation, which considers interphase forces between gas (g) and fuel (f) and between solids (s) and fuel (f), in which the “solids” is the sum of other solid materials: ash, sand, and sorbent species:

$$\oint_A \varepsilon_{f,i}\rho_f\mathbf{v}_{f,i}\mathbf{v}_{f,i}\cdot d\mathbf{A} = \int_V \varepsilon_{f,i}\left(\rho_f-\rho_{susp}\right)\mathbf{g}\,dV + \int_V K_{g-f}\left(\mathbf{v}_g-\mathbf{v}_f\right)dV + \int_V K_{s-f}\left(\mathbf{v}_s-\mathbf{v}_f\right)dV \quad (4.16)$$

The first term on the left hand side is the inertia, with gravity, buoyancy, and drag from gas and solids, respectively, on the right hand side. The buoyancy is considered with the suspension density $\rho_{susp} = \varepsilon_g\rho_g + \left(1-\varepsilon_g\right)\rho_s$ to include the effect of both gas and bed material phases. For the drag force between the gas and fuel phases, Huilin-Gidaspow drag model is utilized, which is a combination of Wen-Yu and Ergun drag models (Gidaspow et al., 1992).

In this case, the EMMS drag correction is not being taken into account as it was originally intended for correcting the solid flow fields (main bed materials). Especially at the lower section of the reactor, the solids concentration is high, and the fuel flow is mainly determined by the drag between the fuel and solid phase (bed phase). Applying any correction to the drag between gas and fuel would have insignificant effect.

For the solid phase drag force, Syamlal equation is used with the radial distribution function by Lebowitz (Gidaspow et al., 1991; Lebowitz, 1964). The governing equations are given below.

$$K_{\mathrm{WY}} = \frac{3}{4}C_D\frac{\varepsilon_g\varepsilon_{\mathrm{f},i}\rho_g\left|\boldsymbol{v}_{\mathrm{f},i}-\boldsymbol{v}_g\right|}{d_{\mathrm{f},i}}\varepsilon_g{}^{-2.65} \qquad \varepsilon_g > 0.8 \quad (4.17)$$

$$K_E = 150\frac{\varepsilon_{\mathrm{f},i}\left(1-\varepsilon_g\right)\mu_g}{\varepsilon_g d_{\mathrm{f},i}^2} + 1.75\frac{\rho_g\varepsilon_{\mathrm{f},i}\left|\boldsymbol{v}_{\mathrm{f},i}-\boldsymbol{v}_g\right|}{d_{\mathrm{f},i}} \qquad \varepsilon_g \le 0.2 \quad (4.18)$$

$$K_{\mathrm{g\text{-}f}} = \phi K_E + (1-\phi)K_{\mathrm{WY}} \quad (4.19)$$

$$\phi = arctan[150\cdot 1.75(0.2-\varepsilon_s)]\,\pi^{-1} + 0.5 \quad (4.20)$$

$$C_D = \begin{cases} \dfrac{24}{Re(1+0.15\,Re^{0.68})} & \mathrm{Re} \le 1000 \\ 0.44 & \mathrm{Re} > 1000 \end{cases} \quad (4.21)$$

$$K_{s-f} = \frac{3(1+e)(\pi/2 + C_f\pi^2/8)\varepsilon_s\varepsilon_{f,i}\rho_s\rho_f(d_s + d_{f,i})^2 g_0 |\boldsymbol{v}_s - \boldsymbol{v}_{f,i}|}{2\pi(\rho_s d_s^3 + \rho_f d_{f,i}^3)} \quad 4.22$$

$$g_0 = \frac{1}{\varepsilon_g} + \frac{3 d_s d_{f,i}}{\varepsilon_g^2 (d_s + d_{f,i})} \sum_{j=1}^{M} \frac{\varepsilon_j}{d_j} \quad 4.23$$

4.5 Heterogeneous fuel reactions

As the fuel enters the reactor, the moisture is evaporated and the volatile and tar components are released due to the high temperature from the presence of hot solids and gas. The remaining char is burned in the presence of oxygen or may react with water vapour and carbon dioxide in gasification reactions. The evaporation, devolatilization, tar release, and char combustion processes are occurring simultaneously, but they have indirect effects on each other. For example, during the devolatilization, combustible gases are released, which consume oxygen and thus reduce the combustion rate of char in the locations with high devolatilization rate. Moreover, the moisture content of the fuel affects the devolatilization and tar release rates. With the usual model parameters, the char combustion rate is much slower than the evaporation, devolatilization, and tar release.

The main heterogeneous reaction rates (evaporation, devolatilization, tar release, and combustion of char) have been modelled by the following equations (in kg/m³s):

$$R'''_{wat,i} = a_{wat}\left(\frac{d_{p,i}}{d_{ref}}\right)^{b_{wat}} \exp\left(\frac{-E_{wat}}{RT}\right) w_{wat,i}\varepsilon_{fuel,i}\rho_{fuel,i} \quad 4.24$$

$$R'''_{vol,i} = a_{vol}\left(\frac{d_{p,i}}{d_{ref}}\right)^{b_{vol}} (1 - w_{H2O,i})^{c_{vol}} \exp\left(\frac{-E_{vol}}{RT}\right) w_{vol,i}\varepsilon_{fuel,i}\rho_{fuel,i} \quad 4.25$$

$$R'''_{tar,i} = a_{tar}\left(\frac{d_{p,i}}{d_{ref}}\right)^{b_{tar}} (1 - w_{H2O,i})^{c_{tar}} \exp\left(\frac{-E_{tar}}{RT}\right) w_{tar,i}\varepsilon_{fuel,i}\rho_{fuel,i} \quad 4.26$$

$$R'''_{char,i} = a_{char}\left(\frac{d_{p,i}}{d_{ref}}\right)^{b_{char}} C_{O_2}^{c_{char}} \exp\left(\frac{-E_{char}}{RT}\right) \exp(-d_{char}\,\varepsilon_s)\, w_{char,i}\varepsilon_{fuel,i}\rho_{fuel,i} \quad 4.27$$

In addition to char combustion, the gasification of char by water-gas reaction ($C + H_2O \rightarrow H_2 + CO$) and Boudouard reaction ($C + CO_2 \rightarrow 2\,CO$) have been modelled by using the following correlations using reaction rate units mol/m³s (Petersen and Werther, 2005):

$$r'''_{watg,i} = 235.3\, C_{C,i} C_{H_2O} \exp\left(\frac{-15\,500}{T}\right) \quad 4.28$$

$$r'''_{boud,i} = 7.696 \cdot 10^6\, C_{C,i} C_{CO_2} \exp\left(\frac{-30\,600}{T}\right) \quad 4.29$$

Most of the char consists of carbon. In the oxidation reaction, the carbon in char (C_{char}) combusts to carbon monoxide and carbon dioxide according to Eq. 4.30, in which the p Parameter γ_{char} is a user given input value, which determines the distribution of CO and CO_2 during combustion of char.

$$C_{char} + (1 - 0.5\,\gamma_{char})\, O_2 \rightarrow \gamma_{char}\, CO + (1 - \gamma_{char})\, CO_2 \quad 4.30$$

During the char combustion, elemental sulphur in char is oxidized to SO_2, nitrogen to NO, and hydrogen to H_2O. During the char gasification, elemental sulphur will form H_2S using char hydrogen, nitrogen to N_2 and leftover hydrogen is released as H_2.

4.6 Sorbent modelling

The following figure illustrates the sorbent species and reactions considered in the model:

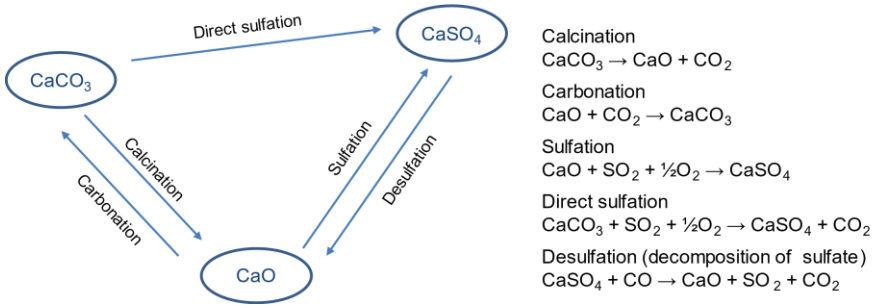

Figure 11. Modelled sorbent species and reactions.

The sorbent material used in this study is Myanit B, an industrial grade calcium carbonate, with a specified size range as illustrated in Figure 8.

The modelled sorbent reactions are:

1) Calcination $CaCO_3 \rightarrow CaO + CO_2$
2) Carbonation $CaO + CO_2 \rightarrow CaCO_3$
3) Indirect sulfation $CaO + SO_2 + 0.5\ O_2 \rightarrow CaSO_4$
4) Direct sulfation $CaCO_3 + SO_2 + 0.5 O_2 \rightarrow CaSO_4 + CO_2$
5) Desulfation $CaSO_4 \rightarrow CaO + SO_2 + 0.5\ O_2$

Continuity equations are defined for each particle size fraction *i* and for each reacting sorbent species *r* ($CaCO_3$, CaO, and $CaSO_4$):

$$\oint_A w_{r,i}\varepsilon_{sorb,i}\rho_{sorb}\mathbf{v}_{sorb,i}\cdot d\mathbf{A} - \oint_A \varepsilon_{sorb,i}\rho_{sorb}D_{sorb,i}\nabla w_{r,i}\cdot d\mathbf{A}$$
$$= \int_V \phi'''_{r,i}\,dV + \int_V R'''_{r,i}\,dV \qquad (4.31)$$
$$- \int_V \sum_{j,j\neq i} w_{r,i}k_{C,sorb,ij}\varepsilon_{sorb,i}\rho_{sorb}\,dV + \int_V \sum_{j,j\neq i} w_{r,j}k_{C,sorb,ji}\varepsilon_{sorb,j}\rho_{sorb}\,dV$$

Eq. 4.31 includes the following terms: 1) convection, 2) dispersion, 3) sources, 4) reactions, 5) comminution to other size fractions, 6) comminution from other size fractions. The term $w_{r,i}$ is a fraction specific weight fraction of species *r*. The velocity field is solved according to Chapter 3.1.

The dispersion constants are defined separately for each furnace zone, each size fraction, and vertical and horizontal directions, but they are the assumed to be the same for all sorbent species.

The different sorbent reactions are controlled by fraction specific reaction rate expressions for each reaction *reac* and reacting sorbent species *r*:

$$R'''_{reac,i} = k_{reac,i}\varepsilon_{r,i}\rho_r \quad (4.32)$$

Table 5 presents the relation between different species (*r*) and reactions (*reac*) and the sign of reaction rate constants (k_{reac}). A negative rate constant indicates the reacting (i.e. consuming) species (e.g. $CaCO_3$ in calcination).

Reaction	Abbr.	Equation	Species (*r*)		
			$CaCO_3$	CaO	$CaSO_4$
Calcination	calc	$CaCO_3 \rightarrow CaO + CO_2$	$-k_{calc}$	$+k_{calc}$	
Carbonation	carb	$CaO + CO_2 \rightarrow CaCO_3$	$+k_{carb}$	$-k_{carb}$	
Sulfation	sulf	$CaO + SO_2 + ½O_2 \rightarrow CaSO_4$		$-k_{sulf}$	$+k_{sulf}$
Direct sulfation	dirs	$CaCO_3 + SO_2 + ½O_2 \rightarrow CaSO_4 + CO_2$	$-k_{dirs}$		$+k_{dirs}$
Desulfation	desu	$CaSO_4 \rightarrow CaO + SO_2 + ½O_2$		$+k_{desu}$	$-k_{desu}$

Table 5. Sign of reaction rate constants k_{reac} for different sorbent species

The species-specific reaction term ($R'''_{r,i}$) in the continuity equation combines the different reactions for each species, for example the reactions defined for $CaSO_4$:

$$\begin{aligned} R'''_{\mathrm{CaSO_4},i} = {} & +k_{sulf,i}\varepsilon_{\mathrm{CaO},i}\,\rho_{\mathrm{CaO}}\frac{M_{\mathrm{CaSO_4}}}{M_{\mathrm{CaO}}} \\ & + k_{dirs,i}\varepsilon_{\mathrm{CaCO_3},i}\,\rho_{\mathrm{CaCO_3}}\frac{M_{\mathrm{CaSO_4}}}{M_{\mathrm{CaCO_3}}} \\ & - k_{desu,i}\varepsilon_{\mathrm{CaSO_4},i}\,\rho_{\mathrm{CaSO_4}} \end{aligned} \quad (4.33)$$

The reaction rate constants are determined by the following correlations, each of which including a tuning parameter *c*, which can be used to match the model results with measurements (note: each of these is defined separately for each size fraction *i*).

Calcination (Khinast et al., 1996):

$$k_{calc} = c_{calc}\,870\,893\,exp\left(\frac{-133\,000}{RT}\right)\,exp\left(-1.38\frac{p_{CO2}}{p_{eq}}\right)\,(1-X_{calc})^{(2/3)} \quad (4.34)$$

Carbonation (Grasa et al., 2008):

$$k_{carb} = c_{carb}\,4.0\,exp\left(\frac{-25\,000}{RT}\right)\,(p_{CO2} - p_{eq})\,(X_{max} - X_{carb})^{(2/3)} \quad (4.35)$$

Equilibrium pressure (Silcox et al., 1989):

$$p_{eq} = 4.137 \cdot 10^7 \exp\left(\frac{-20\,474}{T}\right) \quad (4.36)$$

Sulfation (Myöhänen, 2011):

$$k_{sulf,i} = c_{sulf}\ 20.0\ \exp\left(\frac{-2400}{T}\right)\exp\left(-5.0\ X_{\mathrm{CaSO_4},i}\right) C_{\mathrm{SO_2}} C_{\mathrm{O_2}} M_{\mathrm{CaO}} \qquad \max\left(C_{\mathrm{O_2}}\right) = 0.5\ \mathrm{mol/m^3} \tag{4.37}$$

Direct sulfation (Myöhänen, 2011):

$$k_{dirs,i} = c_{dirs}\ 3.0 \exp\left(\frac{-3031}{T}\right) C_{\mathrm{SO_2}}^{0.9} C_{\mathrm{CO_2}}^{-0.75} C_{\mathrm{O_2}}^{0.001} M_{\mathrm{CaCO_3}} \tag{4.38}$$

Desulfation (Myöhänen, 2011):

$$k_{desu,i} = c_{desu}\ 0.5 \exp\left(\frac{-10\ 000}{T}\right) C_{\mathrm{CO}} M_{\mathrm{CaSO_4}} \tag{4.39}$$

4.7 Homogeneous reactions

The different combustible gaseous species, which are produced from devolatilization, tar release, and char combustion and gasification, burn in the presence of oxygen. In oxygen deficit conditions, the carbon monoxide can react with water vapour to form carbon dioxide and hydrogen in shift conversion, which is a reversible reaction. A species transport equation is defined as follows for all modelled gas species:

$$\oint_A w_r \varepsilon_g \rho_g \mathbf{v}_g \cdot d\mathbf{A} - \oint_A \varepsilon_g \rho_g D_g \nabla w_r \cdot d\mathbf{A} = \int_V \phi_r''' \, dV + \int_V R_r''' \, dV \tag{4.40}$$

The equation includes 1) convection, 2) dispersion, 3) source term, and 4) reaction term. The net velocity field of gas is solved according to Chapter 4.2. The dispersion coefficient (D_g) is empirical. The source term includes the different gaseous feeds. The reaction term includes the species-specific effects of heterogeneous and homogeneous reactions. The modelled homogeneous reaction equations are given below.

$C_7H_8 + 9\ O_2 \rightarrow 7\ CO_2 + 4\ H_2O$ 4.41

$C_2H_4 + 3\ O_2 \rightarrow 2\ CO_2 + 2\ H_2O$ 4.42

$CH_4 + 2\ O_2 \rightarrow CO_2 + 2\ H_2O$ 4.43

$H_2S + 1.5\ O_2 \rightarrow SO_2 + H_2O$ 4.44

$CO + 0.5\ O_2 \rightarrow CO_2$ 4.45

$H_2 + 0.5\ O_2 \rightarrow H_2O$ 4.46

$CO + H_2O \leftrightarrow CO_2 + H_2$ 4.47

The kinetic reaction rates (mol/m^{3}s) of homogeneous combustion reactions are determined as follows:

$$r_{\mathrm{C7H8}}''' = 2.0 \cdot 10^8\ C_{\mathrm{C7H8}} C_{\mathrm{O_2}} \exp\left(\frac{-15\ 000}{T}\right) \tag{4.48}$$

$$r_{C2H4}''' = 2.0 \cdot 10^8\ C_{C2H4} C_{O_2}\ exp\left(\frac{-15\ 000}{T}\right) \tag{4.49}$$

$$r_{CH4}''' = 2.0 \cdot 10^8\ C_{CH4} C_{O_2}\ exp\left(\frac{-15\ 000}{T}\right) \tag{4.50}$$

$$r'''_{H2S} = 1.39 \cdot 10^{9}\, C_{H2S} C_{O_2}\, exp\left(\frac{-18\,956}{T}\right) \quad 4.51$$

$$r'''_{CO} = 3.25 \cdot 10^{7}\, C_{CO} C_{O_2}^{0.5} C_{H_2O}^{0.25}\, exp\left(\frac{-15\,155}{T}\right) \quad 4.52$$

$$r'''_{H2} = 1.08 \cdot 10^{10}\, C_{H2} C_{O_2}\, exp\left(\frac{-15\,034}{T}\right) \quad 4.53$$

The shift conversion is defined as (Biba et al., 1978; Yoon et al., 1978):

$$r'''_{shift} = 2.78\, k_{shift}\, \exp\left(\frac{-1515.46}{T}\right)\left[C_{\mathrm{CO}} C_{\mathrm{H_2O}} - \frac{C_{\mathrm{CO_2}} C_{\mathrm{H_2}}}{0.0265 \exp\left(\frac{3956}{T}\right)}\right] \quad 4.54$$

4.8 Heat transfer

The energy balance and the temperature field of the furnace domain is controlled by Eq. 4.55. It includes:

- convection of gas and solids (line 1),
- dispersion of gas and solids (line 2),
- source terms due to sensible enthalpies of gas and solid sources and additional volumetric heat sources (line 3),
- reaction enthalpies, i.e. heat due to different heterogeneous and homogeneous reactions as a difference between formation enthalpies of products (*pt*) and reactants (*rt*) (line 4),
- direct heat transfer from the cell to the surrounding walls (line 5).

$$\begin{aligned}
&\oint_A \varepsilon_g \rho_g c_{pg} T_c \mathbf{v}_g \cdot d\mathbf{A} + \oint_A \varepsilon_s \rho_s c_{ps} T_c \mathbf{v}_s \cdot d\mathbf{A} \\
&- \oint_A \varepsilon_g \rho_g D_g c_{pg} \nabla T_c \cdot d\mathbf{A} - \oint_A \varepsilon_s \rho_s D_s c_{ps} \nabla T_c \cdot d\mathbf{A} \\
&= \int_V \left(\phi'''_g c_{pg} T_g + \phi'''_s c_{ps} T_s + \varphi'''\right) dV \\
&+ \int_V \left(\sum_{rt} \frac{\partial m'''_{rt}}{\partial t} \frac{H_{0,rt}}{M_{rt}} - \sum_{pt} \frac{\partial m'''_{pt}}{\partial t} \frac{H_{0,pt}}{M_{pt}}\right) dV \\
&- \oint_A \alpha_{cell} (T_{cell} - T_{wall}) \cdot d\mathbf{A}
\end{aligned} \quad 4.55$$

Most of the terms in the energy equation have been solved by the other sub-models, for example, the gas and solid velocities and the reaction rates, or can be directly calculated from the solved parameters, such as the local heat capacities of solid and gas from the solved compositions. The heat transfer in return loop systems, i.e. separators, external heat exchangers and return legs, are solved in separate sub-models and the effects are included to the energy equation, for example as a source of solids from return legs. The dispersion terms simulate the diffusion of energy within the suspension due to transient fluctuation and local mixing of gas and solids and due to radiation. The total heat transfer to walls is combined of convective and radiative heat transfer from the cell next to the wall (dilute phase) and convective heat transfer from the wall layer (dense phase), which is solved by a separate submodel. This attempts to simulate the main heat transfer modes, which occur in CFB furnaces (Figure 12). In the DFB reactors, the wall structure is different and there is no cooling by the membrane wall. However, there is cooling

due to heat loss through the wall structure and the heat transfer phenomena inside the reactor are essentially the same as in a usual CFB boiler.

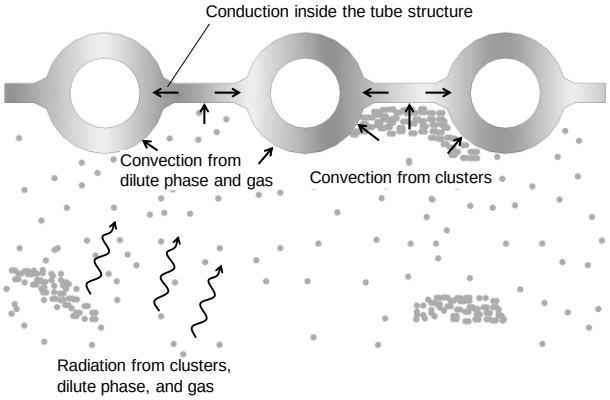

Figure 12. Main heat transfer modes in a circulating fluidized bed reactor.

The heat transfer coefficient α_{cell} includes convective and radiative components:

$$\alpha_{cell} = \alpha_{conv} + \alpha_{rad} \quad (4.56)$$

The convective heat transfer is solved from

$$Nu = Ar^{0.25}\sqrt{\varepsilon_s} \quad (4.57)$$

The radiative heat transfer is defined by the effective emissivity factor

$$\alpha_{rad} = \frac{\varepsilon_{eff}\sigma(T_{cell}^4 - T_{wall}^4)}{T_{cell} - T_{wall}} \quad (4.58)$$

If the temperature difference between the cell and the wall approaches zero (< 1 K), this is replaced by the following expression to avoid divide by zero:

$$\alpha_{rad} = \frac{\varepsilon_{eff}\sigma(T_{cell} + T_{wall})^3}{2} \quad (4.59)$$

In addition, the heat flux to walls includes heat transfer from the superimposed wall layer. In the main computational cells (core), the enthalpy exchange to/from the wall layer occurs via the convective term in the energy equation. The heat flow from wall layer to wall is convective, and the heat transfer coefficient is solved from the same Nusselt equation as above, but the volume fraction of solids at the wall layer is higher, according to Eq. 4.4.

The total heat flux is then

$$q''_{tot} = (\alpha_{conv} + \alpha_{rad})(T_{cell} - T_{wall}) + \alpha_{wl}(T_{wl} - T_{wall}) \quad (4.60)$$

In the model, the given input parameter is the fluid temperature or the “cold temperature” on the other side of the wall and the wall temperatures are solved. The local wall structure can be specified for each cell face in the model as composing of a refractory lining and a wall. The effective thermal transmittance for the wall structure is

$$\frac{\lambda_{eff}}{s_{eff}} = \left(\frac{s_{refr}}{\lambda_{refr}} + \frac{s_{wall}}{\lambda_{wall}}\right)^{-1} \quad 4.61$$

The heat flux through the wall structure (from the hot surface to cold surface) is

$$q''_{tot} = \frac{\lambda_{eff}}{s_{eff}}(T_{wall} - T_{cold}) \quad 4.62$$

The wall temperature is then solved from Eq. 4.60 and 4.62.

5 CFD studies

Ansys Fluent was utilized to study the fluid dynamics of the gasifier at the pilot scale. The subsequent section provides an overview of the computational mesh used for the calculations. The mesh structure was similar to what was applied in the 3D-model to improve the data exchange between the models and to avoid any errors due to interpolation between different meshes. Calculation cell size varied 13…27 mm and the number of cells was 11 128.

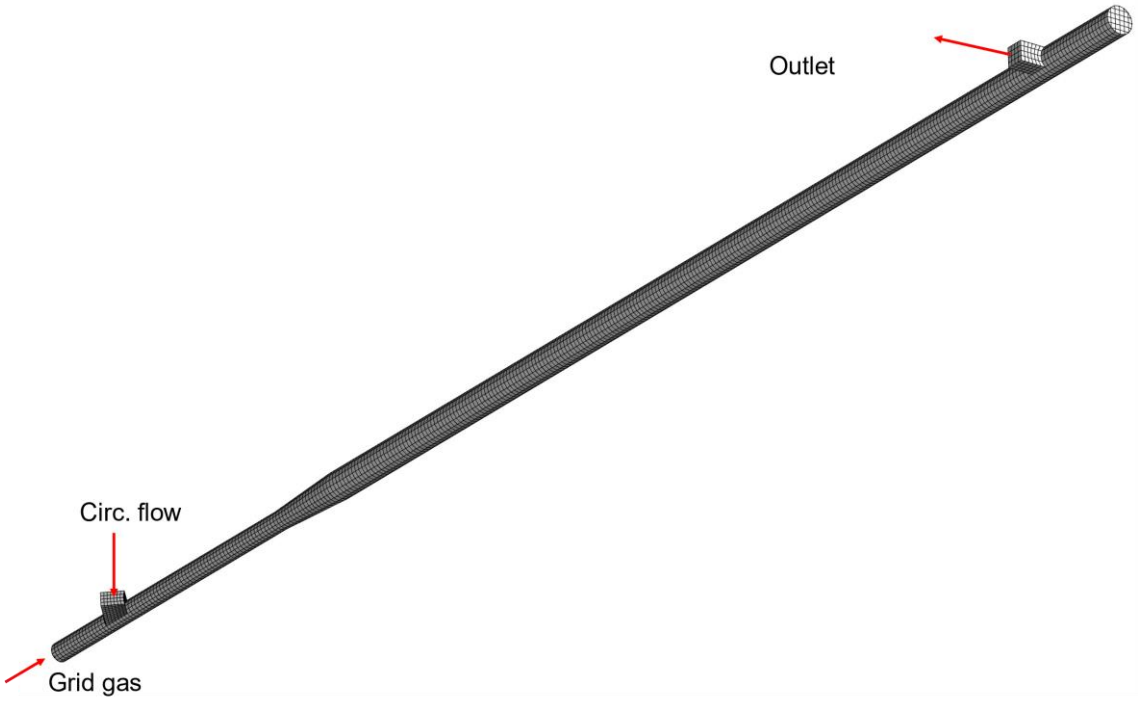

Figure 13. Calculation mesh used in CFD studies.

The CFD-model did not include any reactions, but the gas sources due to reactions (mainly evaporation and devolatilization) were defined as volumetric source terms for the frustum section. This was based on the model results of the 3D-model (Figure 14). With this approach, the average gas velocities in the different parts of the reactor approximated the real conditions.

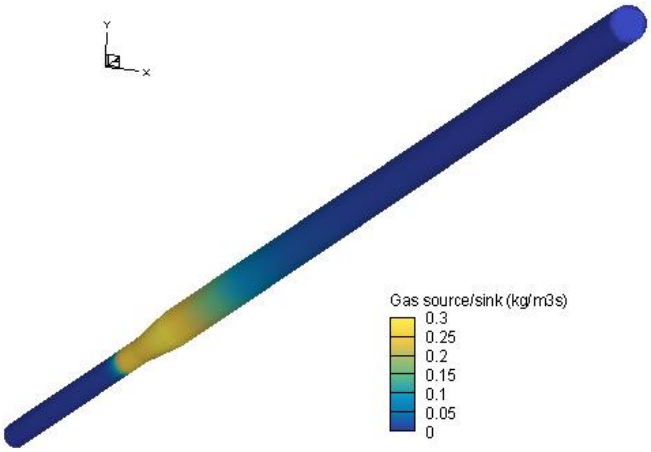

Figure 14. Gas sources due to reactions in the 3D-model, case 18/26E.

The simulation was isothermal with gas density set to 0.252 kg/m^3 and dynamic viscosity 3.81·10^{-5} kg/ms corresponding with the average reactor temperature of 720°C and the average gas composition based on experiments.

The simulations were started with the basic drag models (Wen&Yu) and by first filling the reactor with the bed material. According to VTT, the approximate bed inventory in the pilot tests was 12 kg, which was selected as the target. The bed material was divided into Myanit B (70%) and sand (30%). In the initial simulations, the mean particle sizes were applied: 480 µm and 355 µm for Myanit and sand, respectively.

The initial calculations failed: the simulation ended up with a divergence soon after the EMMS drag model was turned on. The EMMS model was re-evaluated by CERTH and updated UDF-routines were provided. In addition, in the Fluent-model, the time step was reduced from 1 ms to 0.5 ms, and some of the under-relaxation factors were reduced. With the modification, CERTH continued the calculation of the initial case for 12 seconds of the process time. Based on the monitored variable residuals, the simulation was working: the result was converged in each time step. However, the result was not reasonable, as shown in Figure 15. The bed mass was concentrated in a few clusters and the bottom and top of the reactor were practically void of bed particles.

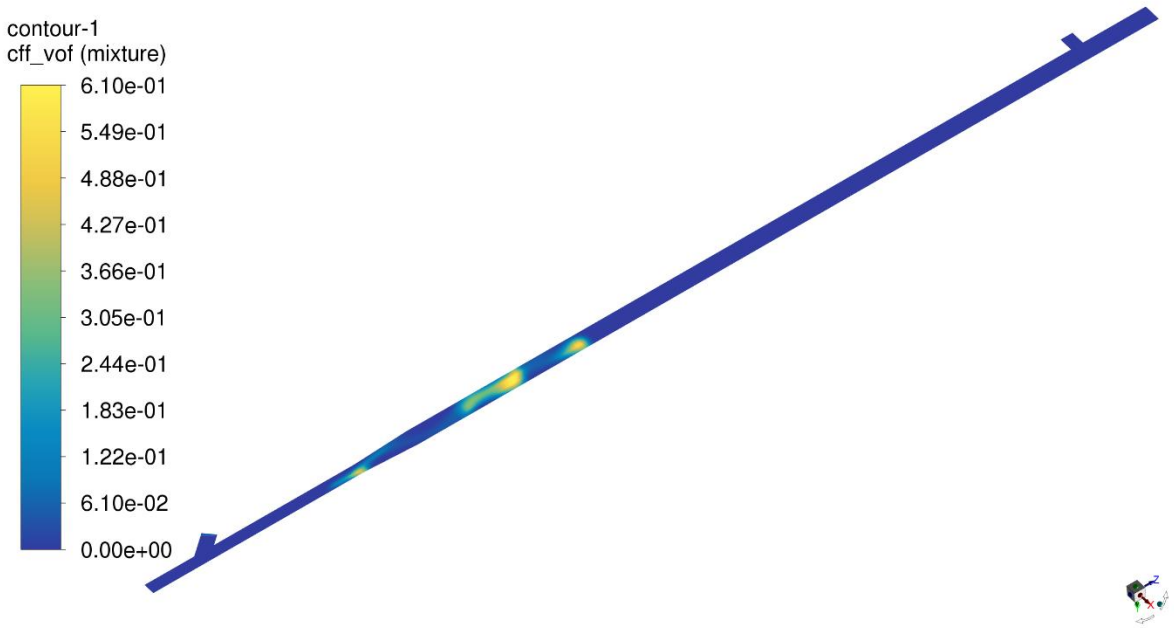

Figure 15. Volume fraction of solids in the initial trial with EMMS drag model by CERTH.

For the next trial, the calculation concept was changed. The total bed masses of Myanit B and sand were controlled by a User Defined Function. Again, the simulation was first initialized with a standard drag model, then switched to apply the updated EMMS drag model. This time, the resulting solid concentration profiles and flow fields appeared to be more reasonable. Figure 16 presents an instantaneous volume fraction of solids at the end of the simulation and Figure 17 presents the time-averaged volume fraction of solids after 10 seconds of simulated process time. The instantaneous result shows, how the bed material tends to flow in dense clusters. The time-averaged profile indicates that the solid concentration is locally higher at the bottom of the reactor, below the entry point of the circulating material. A second zone with higher solid concentration is seen around the frustum. The top of the reactor is mostly void of solids.

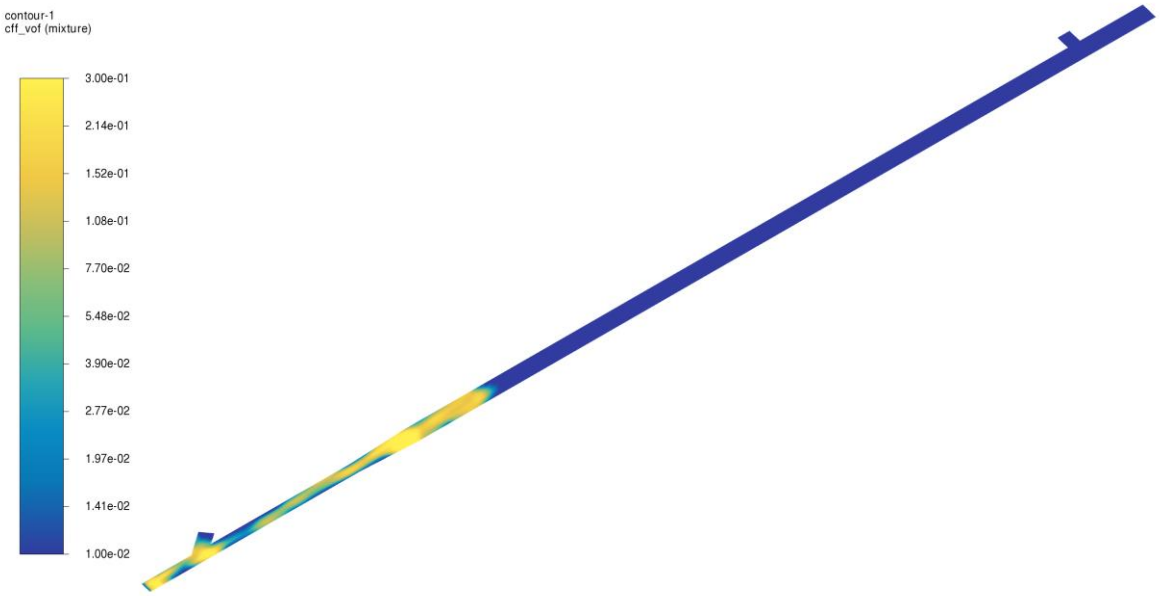

Figure 16. Instantaneous volume fraction of solids with EMMS drag modelling.

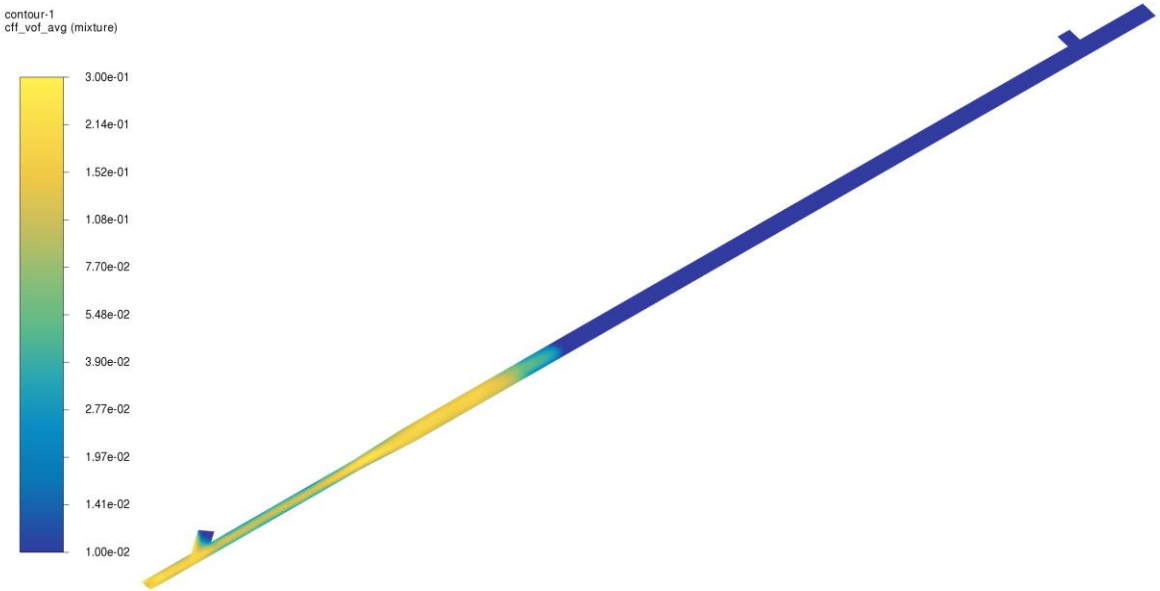

Figure 17. Time-averaged volume fraction of solids with EMMS drag modelling.

For validating the results, the measured pressure profiles of the VTT pilot tests were applied. Figure 18 (left) compares the simulated pressure profile with the measured profiles. Based on the measured profiles, the flow conditions in the four tests have been fairly identical. This is as expected, because the amount of bed material has been the same, and the fluidization velocities and reactor temperatures have been quite similar as well. The repeatability of the measured pressure profiles would indicate that there have not been any random variations between the measurements. The simulated pressure profile indicates a fairly similar result as the measurements. However, when the measured pressure profiles are converted to solid concentration profiles (Eq. 4.5) and compared with the modelled solid concentration profiles, it is evident, that the model fails to simulate the pilot tests accurately (Figure 18, right).

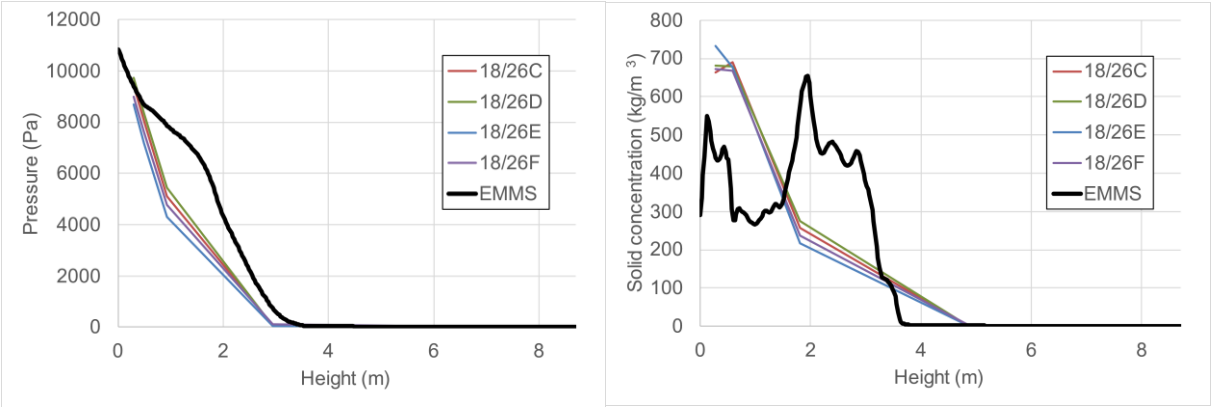

Figure 18. Comparison of measured and simulated pressure profiles and solid concentration profiles. Simulation with EMMS-model.

A common feature with the modelled and measured solid concentration profiles is that the solid concentration is close to zero at the top of the reactor. In the model, this results in zero mass flow of solids out of the reactor. In the pilot measurements, the circulating mass flow rates based on the temperature measurements in the recycling ducts were in the order of 200 g/s. Thus, this was another failure, due to which the EMMS simulations could not be applied as a basis for the reactor model calculations: the whole concept of the indirect steam gasification requires material circulating between the reactors.

The probable reason for the failure was in the original assumption of dividing the bed material to Myanit B and sand and using mean particle sizes to represent the two materials. The reason for reducing the model to only two solid phases was the computational cost. Even with this setting, the calculation was very slow: first, the initialization of the system and reaching stable flow conditions took several days of calculation time. Then achieving just 10 seconds of averaged calculation time took again few days to accomplish. This was further hampered by frequent divergence problems, which were tackled by reducing the calculation time step and under-relaxation factors.

A better approach would have been to divide the bed material into coarse and fine sections: the coarse bed would mostly remain in the reactor, while the fine bed would mostly circulate. New Fluent simulation was prepared by using this approach. Based on the measured particle size distributions, the particle sizes were set to 513 µm and 241 µm, and the bed inventories to 7.464 kg and 4.536 kg for the coarse and fine sections, respectively.

Due to limited resources, updated EMMS drag model correction factors could no longer be defined for this case and the Fluent calculation was performed by using the standard Wen-Yu drag model. Furthermore, a simulation with only 5 seconds of averaging time was achieved, which is probably not sufficient to generate a good enough representation of the steady-state conditions. Figure 19 compares the measured and simulated profiles, when the simulation was based on using coarse and fine bed materials and Wen-Yu model for drag.

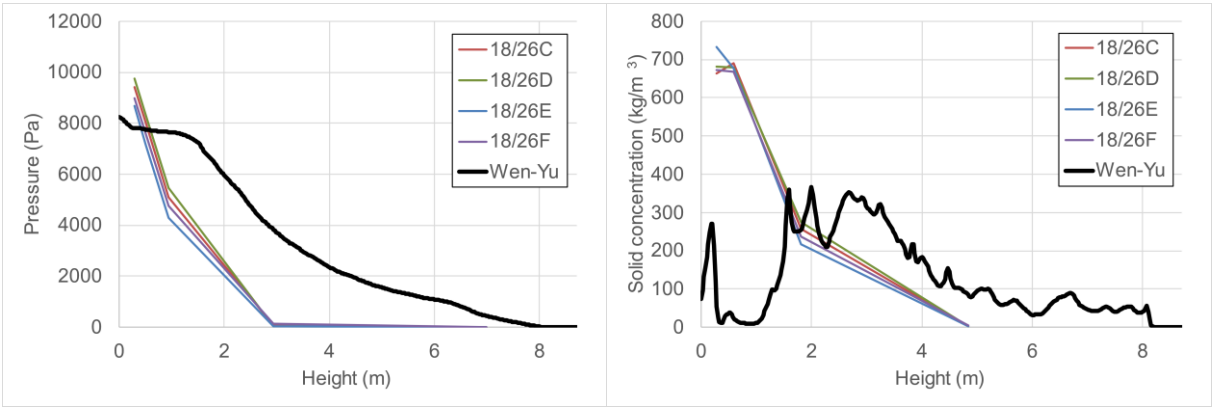

Figure 19. Comparison of measured and simulated pressure profiles and solid concentration profiles. Simulation with Wen-Yu model and using coarse and fine bed materials.

The difference is clear: the fine bed material is able to flow to upper furnace sections as well. However, the profiles do not match the measurements: the amount of bed material is too high at the upper part of the reactor. One possibility is that the pressure measurements of the upper reactor are not valid – after all, there must be some bed material in the upper section as well in order to accomplish circulation of solids. Figure 20 presents the simulated circulating mass flow rate of the fine bed during the last four seconds of the calculation (the first second of the averaging run was lost during the data processing).

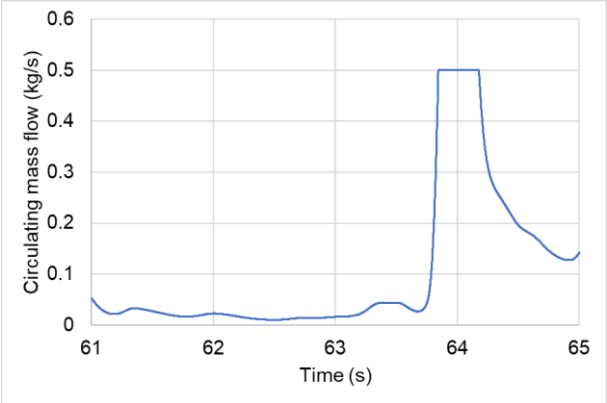

Figure 20. Simulated circulating mass flow rate as a function of time. Simulation with Wen-Yu model and using coarse and fine bed materials.

The variable shown in Figure 20 is the inlet mass flow of the fine bed material (as controlled by the MassControl-UDF). Although the system appeared to be stable before starting the averaging run at 60 seconds of process time, the recorded circulating mass flow shows that at some point, the mass flow out of the system increases suddenly, which results in the high inlet mass flow to maintain the bed inventory. In this simulation, the maximum inlet mass flow was limited to 0.5 kg/s to prevent unrealistically high mass flow rates. After a while, the system stabilizes with a clearly higher circulating mass flow rate: about 150 g/s, which is close to the value defined by VTT.

After spending large resources on CFD simulations, it became clear, that this is not a proper way to achieve fast and reliable simulation results, which was one of the objectives of this task. Due to the iterative nature of the process and the need for continuous adjustments/refinements,and in order to avoid any delays in the linked tasks of the project, the CFD modelling with fine and coarse bed and with EMMS drag model will be investigated later in co-operation with partners, and the results will be reported as a scientific article acknowledging the BioSFerA-project.

6 Modelling of the pilot-scale tests

The modelling of the pilot-scale tests was performed by the semi-empirical 3D-model described in Chapter 4. The test equipment is presented in Figure 21. It consists of an 8.7 m high gasifier, which is coupled with a 6.5 high oxidizer. There is no internal circulation in the reactors, but all the circulating mass flow, which exits one reactor, is introduced to the other reactor. The pilot scale tests that are used for model verification had been performed in 2018 (Table 6).

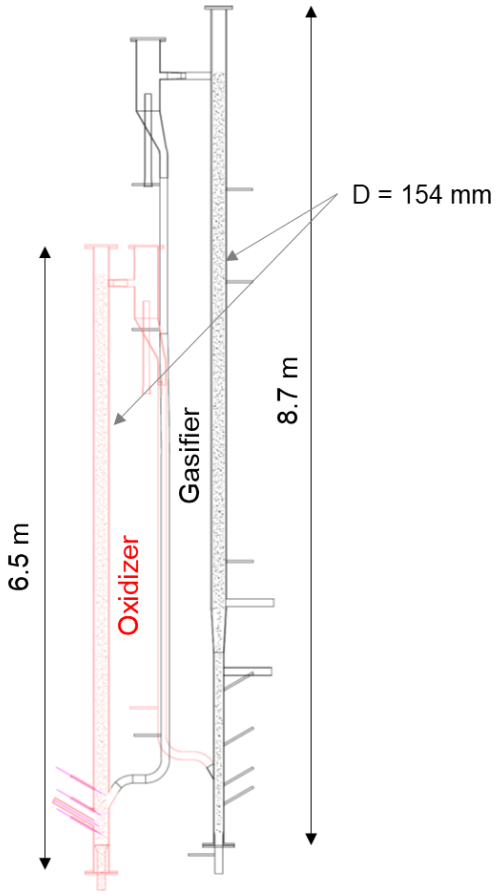

Figure 21. VTT DFB pilot.

Test ID	18/26C	18/26D	18/26E	18/26F
Steam to fuel ratio (kg steam/kg fuel,daf)	1.19	1.11	1.01	1.01
Primary air (g/s)	0.00	1.99	2.00	2.00
Primary oxygen (g/s)	1.20	0.00	0.00	0.00
Primary steam (g/s)	7.00	6.50	6.50	6.50
Purge N_2 (g/s)	2.00	2.00	1.74	1.80
Fuel input (kW)	112	112	122	122
Gasifier outlet temperature. (°C)	764	750	750	739

Table 6. Main process data of pilot scale tests

Because the CFD simulations failed to provide reliable data of the fluid dynamics, the model applied the empirical setting of the bed materials (see Chapter 4.1). A new feature, which was implemented to the model, was the ability to discretize the model geometry by a cut-cell mesh with variable cell sizes (Figure 22).

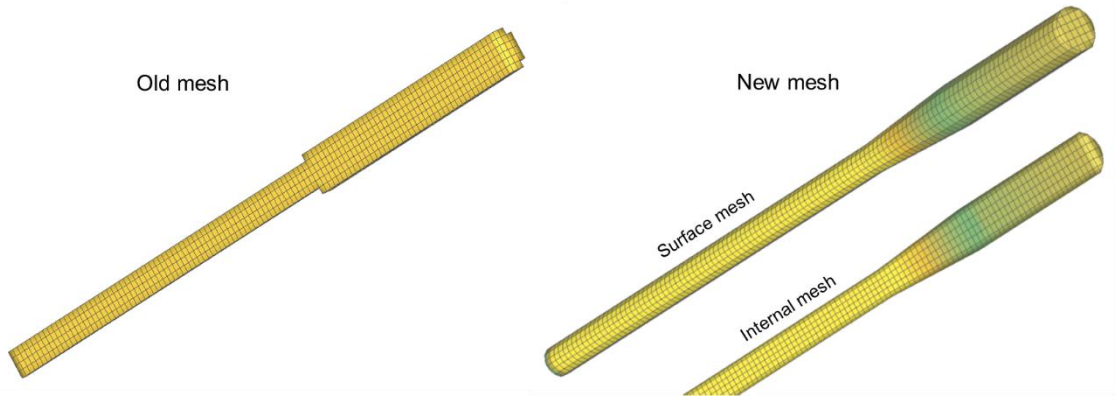

Figure 22. New calculation mesh approach.

The old model applied a fully orthogonal mesh and fixed cell sizes, thus, at the frustum, were the diameter of the reactor increased, this was achieved as a step-wise change in the mesh. With the new mesh, the geometry of the changing reactor diameter could be simulated more accurately. This also improved the convergence, as the cells beside the wall were now aligned on top of each other even in the frustum.

Figure 23 presents the main modelled process variables plotted at the surface of the gasifier. Figure 24 presents the same modelled variables at the mid-plane of the gasifier. The main phenomena, which determine the composition of the producer gas are the evaporation, devolatilization and shift conversion. In the hot conditions of the gasifier, all the moisture and volatiles are released. The highest release rates are near to the feed point. As the resulting gases flow upwards, the composition is largely affected by the shift conversion. In the gasifier conditions, this reversible reaction is only towards increasing the hydrogen content: $CO + H_2O \rightarrow CO_2 + H_2$. The results of the devolatilization and shift conversion profiles are illustreated in the CO and H_2 profiles. Both increase first due to devolatilization. At the upper part of the gasifier, the CO content decreases and the H_2 content further increases due to the shift conversion.

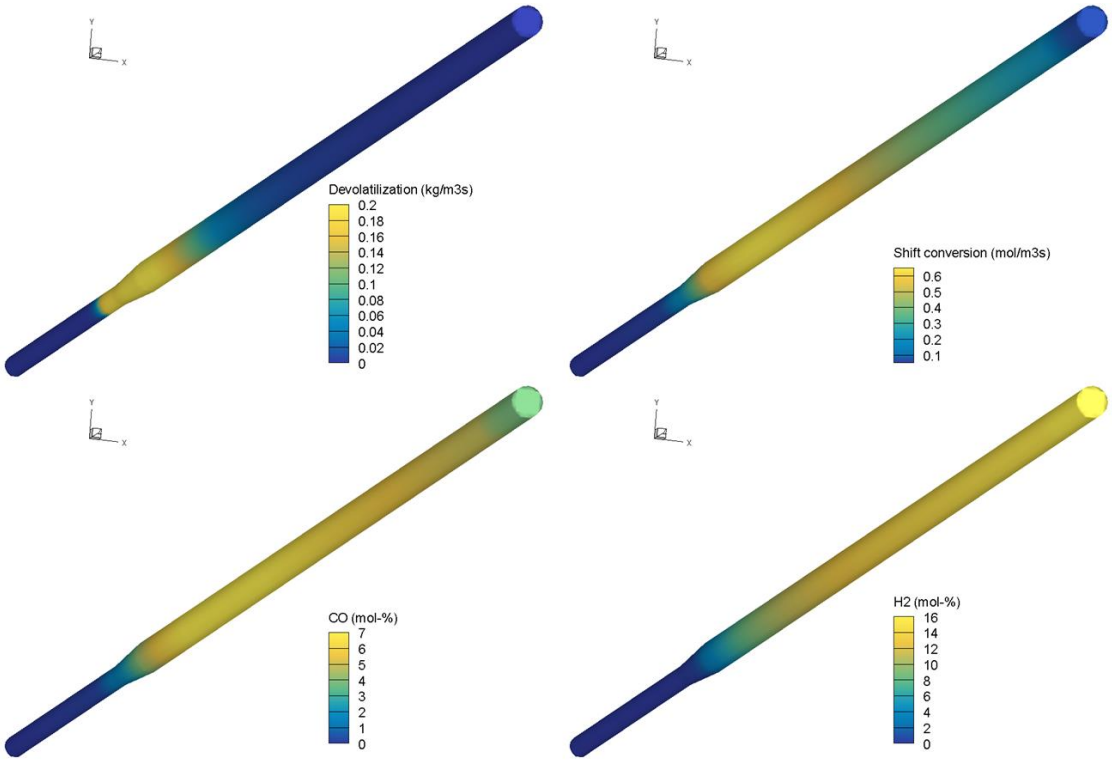

Figure 23. 3D-model results of the gasifier, case 18/26E. Process data at the surface of the gasifier.

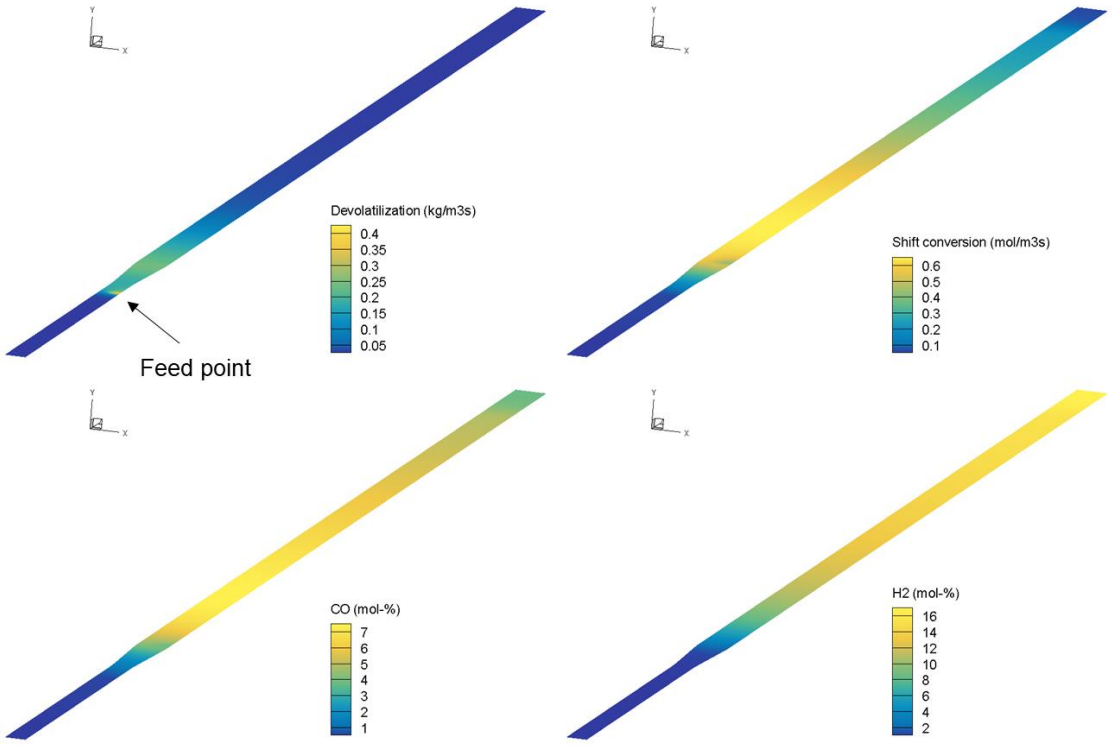

Figure 24. 3D-model results of the gasifier, case 18/26E. Process data at the mid-plane.

Figure 25 compares the measured and modelled producer gas compositions of the pilot tests. In each model case, the different submodel parameters were the same: the differences in the results are just due to changing boundary conditions. The model matches the measurements well. The modelled outlet temperature is higher than the measurement in cases 18/26C and 18/26D. However, in these tests, the electrical heating is clearly higher than in the other tests. This could indicate that in these tests, there have been some unmeasurable heat losses, which have caused the demand for higher electrical heating. In the model, the heat loss to the environment was not tuned separately for different tests, which naturally results in a higher reactor temperature, when the energy input is higher.

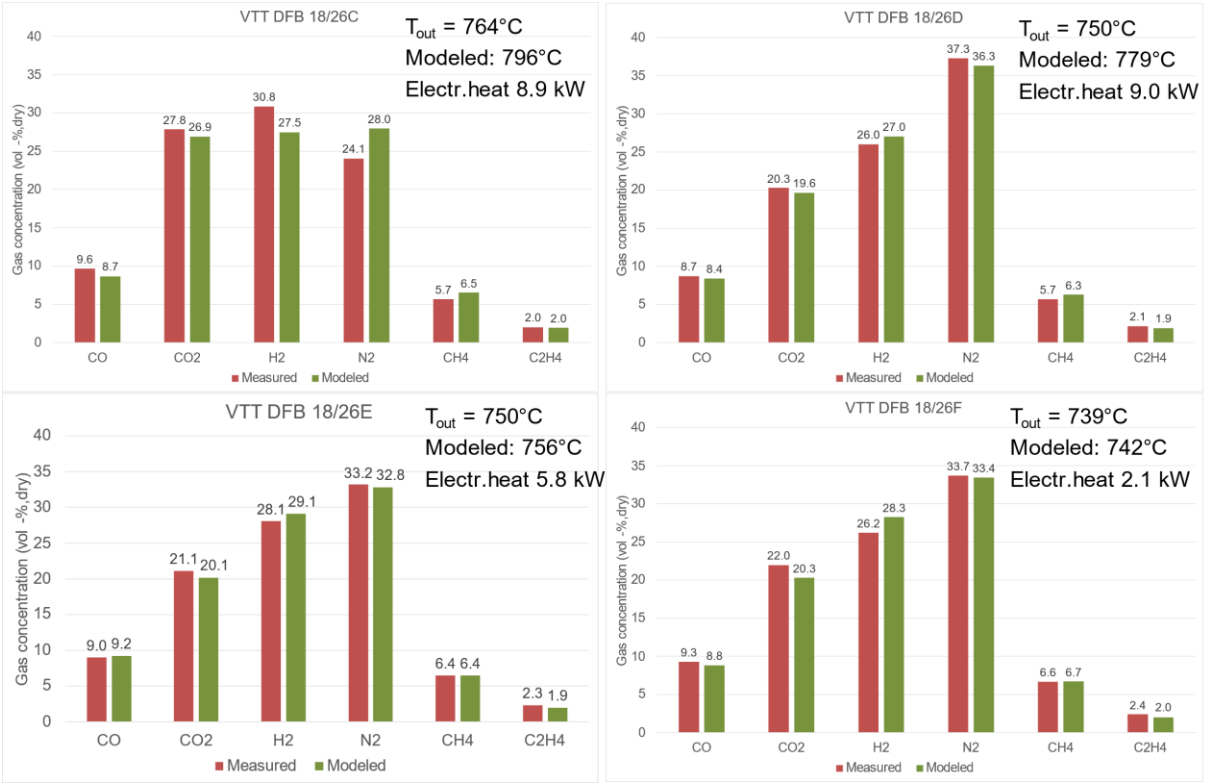

Figure 25. Measured and modelled producer gas compositions of pilot tests.

The calibrated model was applied to simulate the full-scale DFB unit. However, there are some items to be considered when planning the new pilot-scale tests:

- The temperature level in the pilot-scale tests was considerably lower than what was targeted for the full-scale unit. For a better model calibration, the temperature level should be higher, preferably close to 800°C in the gasifier.
- The fluidization gas of the gasifier included air or oxygen. If possible, this should be avoided.
- The chemical composition and particle size distribution of the material circulating between the reactors would be very valuable information for the validation and calibration purposes. If sampling of these material flows can be arranged, it would increase the confidence on the model results.
- Efforts should be made to minimize or avoid the utilization of electrical heating to achieve the desired reaction temperatures within the reactors.

7 Modelling of the full-scale unit

The initial dimensioning of the full-scale unit was defined by SFW for the gasifier and the oxidizer. Based on the initial model results and tuning for suitable fluidization velocities, the diameter of both reactors was slightly adjusted.

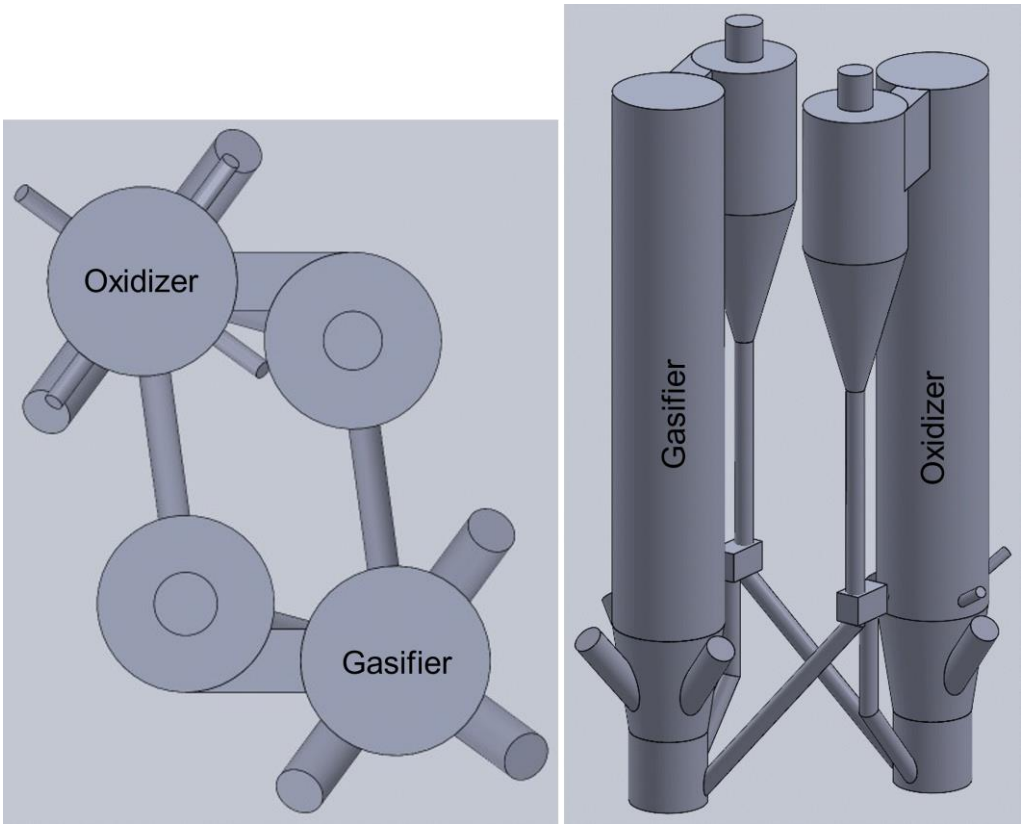

Figure 26. Design of the full-scale unit.

The fuel for the full-scale unit was wood chips (see Table 4 for details). The fuel input was set to 100 MW_{th} with approx.. 5% of the feed directed to the oxidizer. The reactor pressures in the gasifier and the oxidizer were slightly elevated. The bed material was a mixture of sand and limestone. The particle size of the bed was considerably finer than in the pilot scale tests: particle size range 0.1 – 0.6 mm. The feed flow rate of the bed material was set to 1.5% of the fuel feed flow rate.

The plant size falls within the range specified in the grant agreement (100-300 MWth), although it is half the size defined in D.2.4. Indirect gasification is a relatively new concept compared to other gasification technologies like oxy-steam, and there are only a limited number of large-scale operational or designed units. To the best of our knowledge, the largest dual fluidized bed (DFB) facility has been designed for capacities ranging from 15 to 30 MW_{th}. Thus. to mitigate any potential scalability risks, it is recommended to pursue a more realistic design for this indirect gasification unit, targeting a plant size of 100 MW_{th}. SFW will be able to provide process layout and cost engineering for a 100 MW_{th} gasification plant in task 6.3.

The calculation mesh is shown in Figure 27. Since the dimensions of the two reactors were identical, the same mesh was applied for both reactors. The number of cells was 25 744 and the cell size was about 0.2 m. The locations of the different feeds are shown in the same figure. In both reactors, the circulating material from the other reactor is introduced at the lower part of the dense bed area. The fuel feed to the gasifier is handled by three inlets located in the middle of the frustum. In the oxidizer, the fuel feed is much smaller, so only two inlets are applied.

Secondary air is introduced above the fuel feeds after the frustum. In the initial studies, the number of secondary air nozzles was just two and located above the fuel feeding points, but this caused a low combustion efficiency as the char from the gasifier could easily bypass the secondary air feed level on the front side of the reactor.

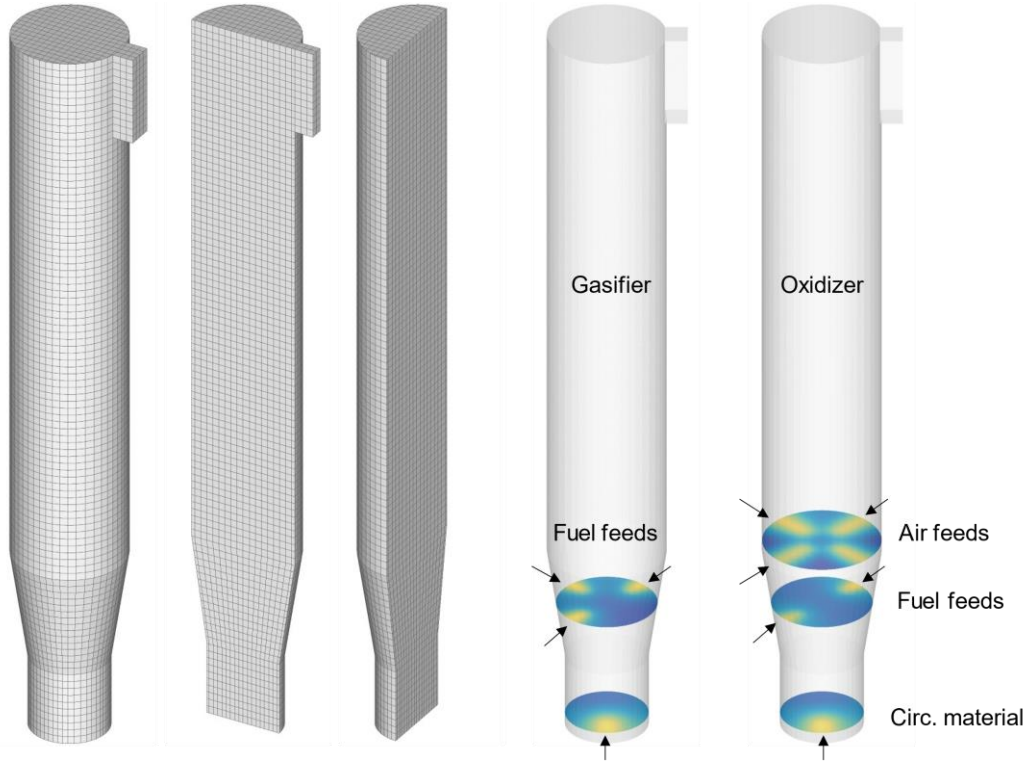

Figure 27. Calculation mesh of the full-scale unit and the location of feeds.

Figure 28 visualizes the modelled composition fields of the main gas components in the gasifier. The profiles coincide with the location of the fuel feeds, i.e. the components originating from fuel are higher on the side of the fuel feeds.

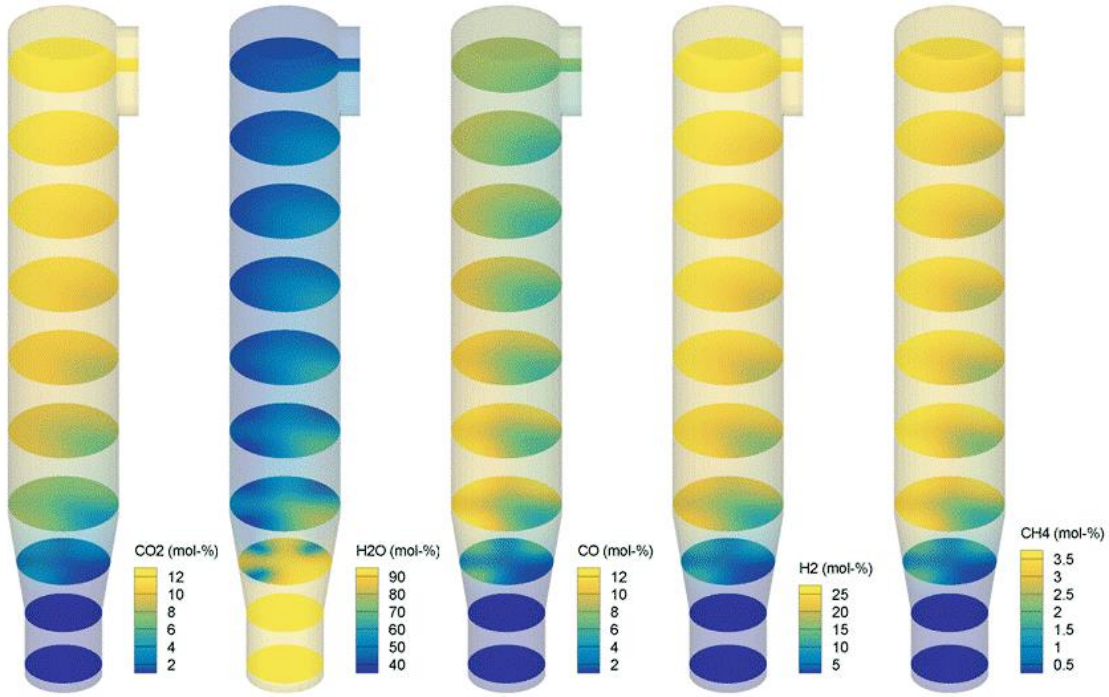

Figure 28. Modelled gas composition fields of the full-scale gasifier.

Similar to the pilot-scale gasifier, the producer gas composition is mostly affected by evaporation, devolatilization and shift conversion. The devolatilization, water-gas reaction with char, and shift conversion profiles are shown in Figure 29. The evaporation rate profile would be similar to the devolatilization profile. Like before, the devolatilization rate is highest near to the fuel feeding points, while the shift conversion is affecting in a larger volume at the upper section of the gasifier. There is some water-gas reaction of the char close to the fuel feeding points, but the net effect of this is insignificant compared with devolatilization and shift conversion.

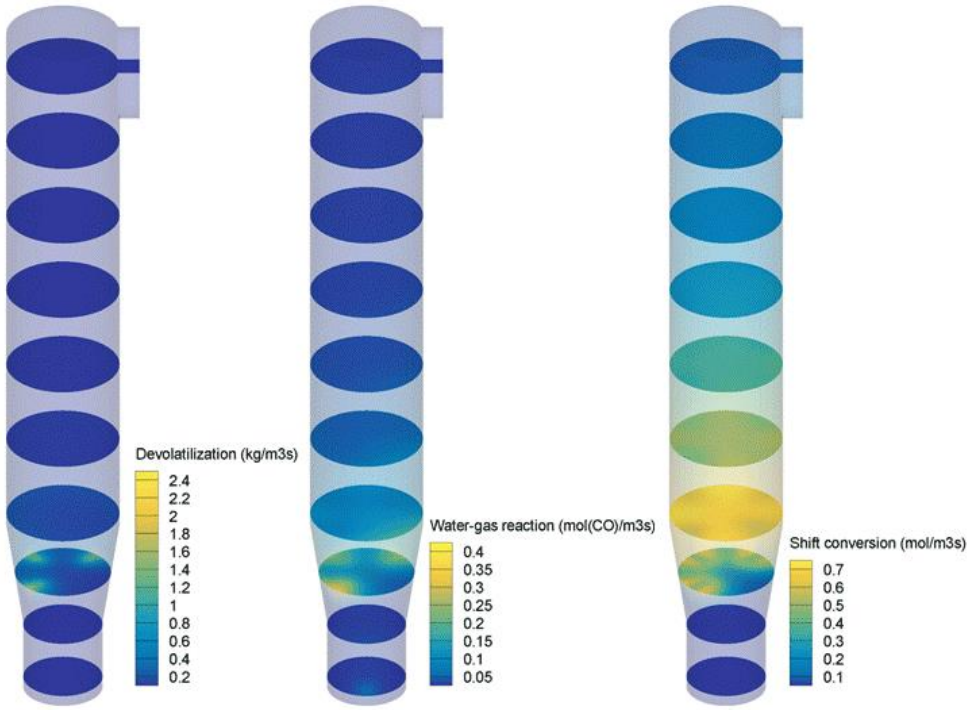

Figure 29. Modelled reaction rates of the full-scale gasifier.

The main gas components inside the oxidizer together with the char concentration fields are presented in Figure 30. The excess oxygen concentration was adjusted by the air feed flow rates to the desired level. The oxygen profile shows, how the oxygen of the grid air is depleted by the combustion reactions of char at the bottom of the reactor. The circulating material entry at the front side of the reactor results in a non-uniform oxygen profile below the secondary air inlets. At the upper section of the reactor, the oxygen profile is quite uniform, which results in good combustion efficiency. The CO_2-profile is almost a mirror image of the O_2-profile, which is due to the combustion reactions and air inlets. At the bottom section of the oxidizer, the CO content is high, but after the secondary air level, the combustible gases are burned and the amount of CO in the flue gas is low. The char concentration profile shows how the char is spreading from the inlet point and is efficiently burned.

Figure 31 compares the gas velocity and temperature fields in the gasifier and the oxidizer. Both reactors are well insulated, so the temperature profile is a result of the circulating material feeds and the reactions. In the gasifier, the temperature is locally higher at the entry point of the hot circulating material originating from the oxidizer. After that, the temperature is decreasing due to endothermic reactions (mainly evaporation and devolatilization). The shift conversion is slightly exothermic, but it does not have a large effect on the temperature profile. In the oxidizer, the entry point of the cold circulating material from the gasifier is clearly seen at the bottom of the reactor. Most of the combustion reactions occur at the lower section of the oxidizer resulting in almost constant temperature at the upper parts of the oxidizer.

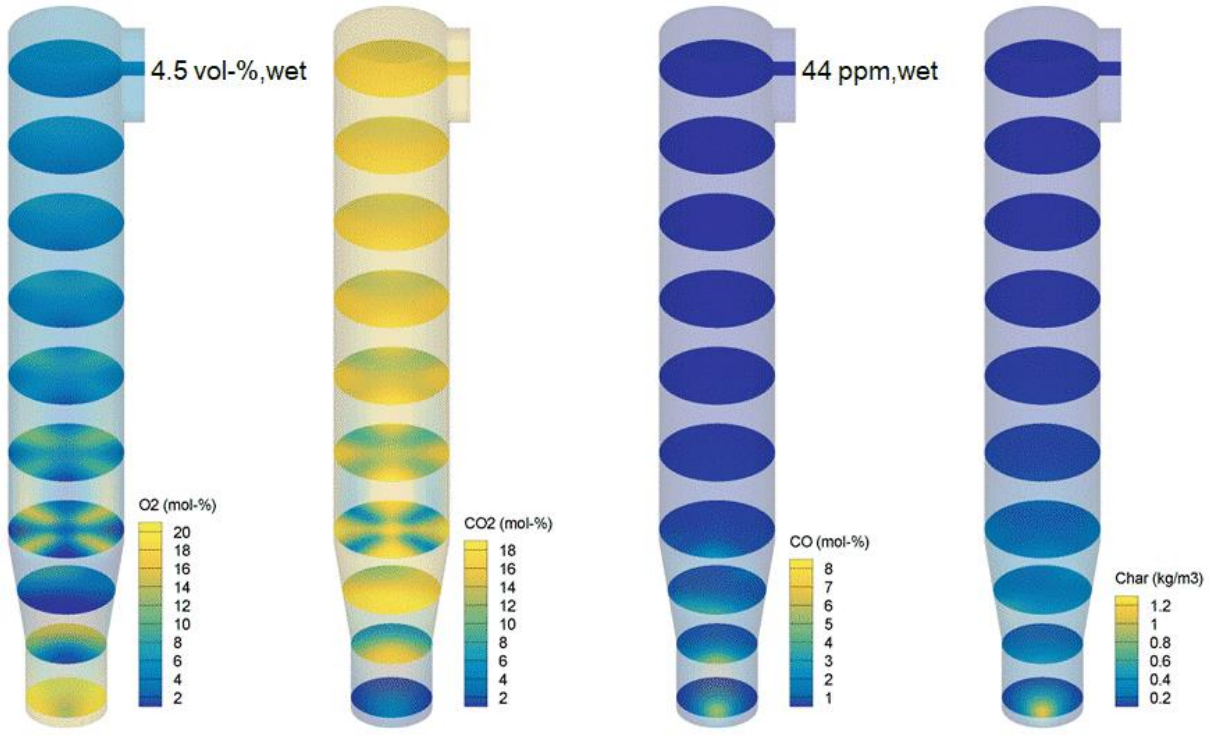

Figure 30. Modelled gas composition fields and char concentration fields of the full-scale oxidizer.

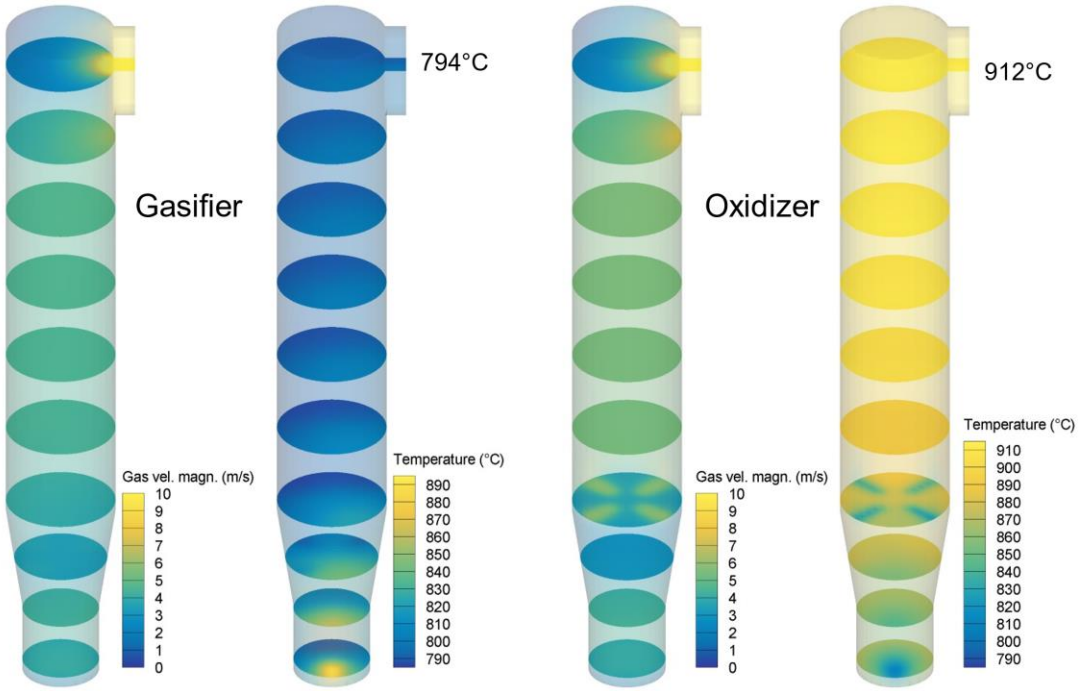

Figure 31. Modelled gas velocity magnitude and temperature in the gasifier and the oxidizer.

The producer gas composition is visualized in Figure 32. The H_2/CO-ratio is about 3.5, which is slightly higher than in the pilot scale studies (≈3.2). This is mostly due to higher shift conversion rate in pressurized conditions. Besides the pressure, the main difference between the full-scale and pilot-scale units is that in the full-scale, no oxygen was fed into the gasifier, thus, the oxidation reactions were prevented. Moreover, the share of purge nitrogen was smaller, which reduced the amount of nitrogen in the producer gas. Furthermore, the gasifier temperature was higher, 794°C vs. 750°C, which affects the different reactions.

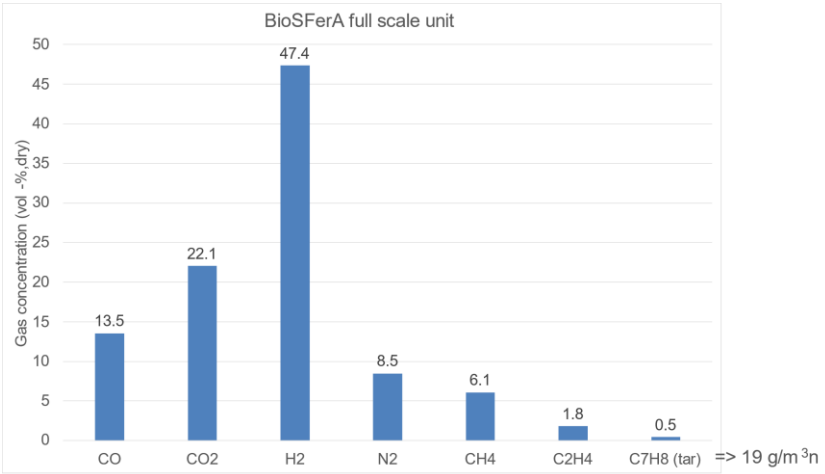

Figure 32. Producer gas composition of the full-scale gasifier.

8 Tabled process data

The following tables present the modelled process data of the pilot-scale tests and the full-scale simulation.

8.1 Producer gas composition

Gas (vol-%,wet)	18/26C	18/26D	18/26E	18/26F	Full-scale
O_2	0	0	0	0	0
CO_2	12.11	10.26	10.80	10.83	11.90
H_2O	54.99	47.73	46.41	46.68	46.09
SO_2	4.72E-03	4.88E-03	5.31E-03	5.20E-03	2.03E-03
CO	3.90	4.38	4.91	4.70	7.29
H_2	12.37	14.13	15.60	15.07	25.53
CH_4	2.94	3.30	3.44	3.57	3.28
C_2H_4	0.88	0.99	1.03	1.07	0.98
H_2S	9.59E-04	9.58E-04	1.01E-03	1.00E-03	3.28E-04
NH_3	0.044	0.043	0.046	0.046	0.105
N_2	12.58	18.98	17.57	17.83	4.57
C_7H_8	0.182	0.180	0.192	0.192	0.244
T (°C)	799	782	759	747	794
q_m (kg/s)	0.0167	0.0169	0.0172	0.0173	9.340

Table 7. Producer gas composition after the gasifier. Temperature and mass flow at reactor exit.

8.2 Flue gas composition

Gas (vol-%,wet)	18/26C	18/26D	18/26E	18/26F	Full-scale
O_2	5.70	3.55	1.93	3.12	4.55
CO_2	14.77	16.89	18.50	17.26	15.59
H_2O	0.30	0.35	0.38	0.36	2.04
SO_2	4.39E-04	4.26E-04	1.07E-03	5.21E-04	1.12E-04
CO	0.108	0.120	0.135	0.170	4.38E-03
H_2	0	0	0	0	0
CH_4	0	0	0	0	0
C_2H_4	0	0	0	0	0
H_2S	0	0	0	0	0
NH_3	0	0	0	0	4.97E-03
N_2	79.12	79.09	79.06	79.10	77.81
C_7H_8	0	0	0	0	0
T (°C)	820	820	826	807	912
q_m (kg/s)	0.0190	0.0174	0.0173	0.0185	17.246

Table 8. Flue gas composition after the oxidizer. Temperature and mass flow at reactor exit.

8.3 Circulating material flows from gasifier

Mass flow (kg/s)	18/26C	18/26D	18/26E	18/26F	Full-scale
Char	0.00169	0.00181	0.00214	0.00213	0.988
Ash	0.09467	0.09596	0.10740	0.09857	51.298
Sand	0.13170	0.11256	0.11266	0.12085	60.916
$CaCO_3$	0	0	0	0	0.000
CaO	0.02455	0.02520	0.02500	0.02477	15.319
$CaSO_4$	0.00020	0.00020	0.00020	0.00021	2.473
MgO	0.01770	0.01817	0.01803	0.01786	0.000
Total	0.271	0.254	0.265	0.264	131.0
T (°C)	798	782	770	746	794

Table 9. Circulating mass flows from gasifier to oxidizer.

Share (wt-%)	18/26C	18/26D	18/26E	18/26F	Full-scale
Char	0.62	0.71	0.81	0.80	0.75
Ash	35.00	37.79	40.46	37.28	39.16
Sand	48.69	44.33	42.45	45.71	46.50
$CaCO_3$	0	0	0	0	0.00
CaO	9.07	9.92	9.42	9.37	11.69
$CaSO_4$	0.07	0.08	0.07	0.08	1.89
MgO	6.54	7.16	6.79	6.76	0.00

Table 10. Distribution of material species of circulating mass flows from gasifier to oxidizer.

8.4 Circulating material flows from oxidizer

Mass flow (kg/s)	18/26C	18/26D	18/26E	18/26F	Full-scale
Char	0.00061	0.00069	0.00092	0.00090	0.050
Ash	0.09467	0.09586	0.10742	0.09856	51.298
Sand	0.13176	0.11255	0.11303	0.12093	60.977
$CaCO_3$	0.00002	0.00002	0.00002	0.00004	0.000
CaO	0.02457	0.02520	0.02521	0.02479	15.325
$CaSO_4$	0.00020	0.00020	0.00020	0.00021	2.485
MgO	0.01773	0.01818	0.01819	0.01789	0.000
Total	0.270	0.253	0.265	0.263	130.1
T (°C)	820	820	826	807	912

Table 11. Circulating mass flows from oxidizer to gasifier.

Share (wt-%)	18/26C	18/26D	18/26E	18/26F	Full-scale
Char	0.23	0.27	0.35	0.34	0.04
Ash	35.12	37.93	40.54	37.43	39.42
Sand	48.88	44.54	42.65	45.93	46.86
$CaCO_3$	0.01	0.01	0.01	0.01	0.00
CaO	9.12	9.97	9.52	9.41	11.78
$CaSO_4$	0.07	0.08	0.08	0.08	1.91
MgO	6.58	7.19	6.86	6.80	0.00

Table 12. Distribution of material species of circulating mass flows from oxidizer to gasifier.

9 Conclusions

This deliverable reports the modelling activities conducted in Task 6.1, the primary goal of which was to establish a robust and efficient model system for simulating dual fluidized bed (DFB) gasification. Validation and calibration of the model were accomplished using the pilot-scale tests carried out by VTT.

CERTH developed an Energy Minimization Multi-Scale (EMMS) drag sub-model to enhance the accuracy of simulations of fluid dynamics under the specific operational conditions of the pilot-scale DFB unit. Ansys Fluent's multiphase model, based on the Kinetic Theory of Granular Flow (KTGF), was utilized to study the fluid dynamics of the pilot gasifier. However, CFD modelling based on both the standard Wen-Yu drag model and the EMMS drag model did not successfully replicate the experiments. These models also showed a high computational cost, even under simplified assumptions, and exhibited susceptibility to divergence problems.

The reactor model calculations were performed by a 3D-model based on empirically set solid concentration profiles. Reaction submodels were calibrated based on the pilot-scale tests, using a consistent set of parameters for each simulation. The modelled gas compositions and reactor temperatures showed a high degree of correlation with the measurements.

With the calibration completed, the model was used to simulate a full-scale (100 MW_{th}) DFB unit. The initial reactor dimensions were adjusted according to the model results. In addition, the placement of different feeds was adjusted supported by the model.

The main objective of creating a feasible model for the study of DFB gasification was successfully achieved. The calibrated model can be applied to examine the full-scale unit under various process conditions.

10 References

Adamczyk, W.P., Myöhänen, K., Hartge, E.U., Ritvanen, J., Klimanek, A., Hyppänen, T., Białecki, R.A., 2018. Generation of data sets for semi-empirical models of circulated fluidized bed boilers using hybrid Euler-Lagrange technique. Energy 143, 219–240. https://doi.org/10.1016/j.energy.2017.10.029

Biba, V., Macák, J., Klose, E., Malecha, J., 1978. Mathematical Model for the Gasification of Coal under Pressure. Ind. Eng. Chem. Process Des. Dev. 17, 92–98. https://doi.org/10.1021/i260065a017

BioSFerA, 2020. BioSFerA - Biofuel for Biotravel [WWW Document]. URL https://biosfera-project.eu/ (accessed 5.24.23).

Chen, C., 2015. Investigations on Mesoscale Structure in Gas–Solid Fluidization and Heterogeneous Drag Model. Springer Berlin, Heidelberg. https://doi.org/10.1007/978-3-662-48373-2

European Commission, 2017. Scale-up of Calcium Carbonate Looping Technology for Efficient CO2 Capture from Power and Industrial Plants | SCARLET Project | Fact Sheet | FP7 | CORDIS | European Commission. [WWW Document]. URL https://cordis.europa.eu/project/id/608578 (accessed 5.24.23).

FlexFlores, 2019. HomePage | Flex Flores [WWW Document]. URL https://www.flex-flores.eu/ (accessed 5.24.23).

Gidaspow, D., 1994. Multiphase Flow and Fluidization: Continuum and Kinetic Theory Description. Academic Press.

Gidaspow, D., Bezburuah, R., Ding, J., 1992. Hydrodynamics of circulating fluidized beds: Kinetic theory approach, in: Potter, O.E., Nicklin, D.J. (Eds.), 7th Fluidization Conference. Engineering Foundation, New York, pp. 75–82.

Gidaspow, D., Bezburuah, R., Ding, J., 1991. Hydrodynamics of circulating fluidized beds: Kinetic theory approach., in: 7th International Conference on Fluidization, Gold Coast (Australia).

Grasa, G.S., Abanades, J.C., Alonso, M., González, B., 2008. Reactivity of highly cycled particles of CaO in a carbonation/calcination loop. Chem. Eng. J. 137, 561–567. https://doi.org/10.1016/j.cej.2007.05.017

Johnsson, F., Leckner, B., 1995. Vertical distribution of solids in a CFB-furnace, in: Heinschel, K.J. (Ed.), Proceedings of the 13th International Conference on Fluidized Bed Combustion. ASME, New York, pp. 671–679.

Khinast, J., Krammer, G.F., Brunner, C., Staudinger, G., 1996. Decomposition of limestone: The influence of CO2 and particle size on the reaction rate. Chem. Eng. Sci. 51, 623–634. https://doi.org/10.1016/0009-2509(95)00302-9

Koski, M., Ritvanen, J., Myöhänen, K., Hyppänen, T., Palonen, J., Häkkinen, K., Kokki, S., 2012. Three-dimensional modelling of steam-oxygen gasification in a circulating fluidized bed, in: Arena, U., Chirone, R., Miccio, M., Salatino, P. (Eds.), Proceedings of the 21st International Conference on Fluidized Bed Combustion. EnzoAlbanoEditore, Naples, pp. 883–890.

Lebowitz, J.L., 1964. Exact solution of generalized Percus-Yevick equation for a mixture of hard spheres. Phys. Rev. 133, A895–A899. https://doi.org/10.1103/PhysRev.133.A895

Li, J., Ge, W., Wang, W., Yang, N., Liu, X., Wang, L., He, X., Wang, X., Wang, J., Kwauk, M., 2013. From Multiscale Modeling to Meso-Science: A Chemical Engineering Perspective. Springer Berlin, Heidelberg. https://doi.org/10.1007/978-3-642-35189-1

Li, J., Kwauk, M., 2003. Exploring complex systems in chemical engineering - The multi-scale methodology. Chem. Eng. Sci. 58, 521–535. https://doi.org/10.1016/S0009-2509(02)00577-8

Myöhänen, K., 2011. Modelling of combustion and sorbent reactions in three-dimensional flow environment of a circulating fluidized bed furnace. LUT University.

Myöhänen, K., Hyppänen, T., 2011. A three-dimensional model frame for modelling combustion and gasification in circulating fluidized bed furnaces. Int. J. Chem. React. Eng. 9, A25. https://doi.org/10.2202/1542-6580.2571

Myöhänen, K., Hyppänen, T., Eriksson, T., Kuivalainen, R., 2014. Design and modeling of second generation oxygen-fired CFB, in: Proceedings of the 11th International Conference on Fluidized Bed Technology. pp. 475–480.

Myöhänen, K., Palonen, J., Hyppänen, T., 2018. Modelling of indirect steam gasification in circulating fluidized bed reactors. Fuel Process. Technol. 171, 10–19. https://doi.org/10.1016/j.fuproc.2017.11.006

Nikku, M., Myöhänen, K., Ritvanen, J., Hyppänen, T., 2014. Three-dimensional modeling of fuel flow with a holistic circulating fluidized bed furnace model. Chem. Eng. Sci. 117, 352–363. https://doi.org/10.1016/j.ces.2014.06.038

Nikku, M., Myöhänen, K., Ritvanen, J., Hyppänen, T., Lyytikäinen, M., 2016. Three-dimensional modeling of biomass fuel flow in a circulating fluidized bed furnace with an experimentally derived momentum exchange model. Chem. Eng. Res. Des. 115, 77–90. https://doi.org/10.1016/j.cherd.2016.09.023

Nikku, M., Zhan, M., Myöhänen, K., Ritvanen, J., Li, X., 2021. Three-dimensional modeling of a chinese circulating fluidized bed incinerator firing municipal solid waste. J. Solid Waste Technol. Manag. 47, 393–405. https://doi.org/10.5276/JSWTM/2021.393

Parkkinen, J., Myöhänen, K., Abanades, J.C., Arias, B., Hyppänen, T., 2017. Modelling a calciner with high inlet oxygen concentration for a calcium looping process. Energy Procedia 114, 242–249. https://doi.org/10.1016/j.egypro.2017.03.1166

Petersen, I., Werther, J., 2005. Experimental investigation and modeling of gasification of sewage sludge in the circulating fluidized bed. Chem. Eng. Process. Process Intensif. 44, 717–736. https://doi.org/10.1016/j.cep.2004.09.001

Silcox, G.D., Kramlich, J.C., Pershing, D.W., 1989. A Mathematical Model for the Flash Calcination of Dispersed CaCO3 and Ca(OH)2 Particles. Ind. Eng. Chem. Res. 28, 155–160. https://doi.org/10.1021/ie00086a005

Syamlal, M., 1987. The particle-particle drag term in a multiparticle model of fluidization. DOE/MC/21353-2373. https://www.osti.gov/biblio/6355923.

Wang, J., Ge, W., Li, J., 2008. Eulerian simulation of heterogeneous gas-solid flows in CFB risers: EMMS-based sub-grid scale model with a revised cluster description. Chem. Eng. Sci. 63, 1553–1571. https://doi.org/10.1016/j.ces.2007.11.023

Wang, W., Li, J., 2007. Simulation of gas-solid two-phase flow by a multi-scale CFD approach-of the EMMS model to the sub-grid level. Chem. Eng. Sci. 62, 208–231. https://doi.org/10.1016/j.ces.2006.08.017

Wen, C.Y., Yu, Y.H., 1966. A generalized method for predicting the minimum fluidization velocity. AIChE J. 12, 610–612. https://doi.org/10.1002/aic.690120343

Yoon, H., Wei, J., Denn, M.M., 1978. A model for moving-bed coal gasification reactors. AIChE J. 24, 885–903. https://doi.org/10.1002/aic.690240515

Zeneli, M., Nikolopoulos, A., Nikolopoulos, N., Grammelis, P., Kakaras, E., 2015. Application of an advanced coupled EMMS-TFM model to a pilot scale CFB carbonator. Chem. Eng. Sci. 138, 482–498. https://doi.org/10.1016/j.ces.2015.08.008